Membership lists for 431 open clusters in Gaia DR2 using extreme deconvolution gaussian mixture models

KARL JAEHNIG (D, 1, 2, 3) JONATHAN BIRD, 1, 4 AND KELLY HOLLEY-BOCKELMANN (D, 5)

 1Department of Physics and Astronomy, Vanderbilt University, Nashville, TN 37235, USA 2Fisk -Vanderbilt Bridge Fellow 3LSSTC Data Science Fellow 4VIDA Fellow 5Department of Physics, Fisk University, Nashville, TN, 37208, USA

ABSTRACT

Open clusters are groups of stars that form at the same time, making them an ideal laboratory to test theories of star formation, stellar evolution, and dynamics in the Milky Way disk. However, the utility of an open cluster can be limited by the accuracy and completeness of its known members. Here, we employ a "top-down" technique, extreme deconvolution gaussian mixture models (XDGMM), to extract and evaluate known open clusters from Gaia DR2 by fitting the distribution of stellar parallax and proper motion along a line-of-sight. Extreme deconvolution techniques can recover the intrinsic distribution of astrometric quantities, accounting for the full covariance matrix of the errors; this allows open cluster members to be identified even when presented with relatively uncertain measurement data. To date, open cluster studies have only applied extreme deconvolution to specialized searches for individual systems. We use XDGMM to characterize the open clusters reported by Ahumada & Lapasset (2007) and are able to recover 420 of the 426 open clusters therein (98.1%). Our membership list contains the overwhelming majority (> 95\%) of previously known cluster members. We also identify a new, significant, and relatively faint cluster member population and validate their membership status using Gaia eDR3. We report the fortuitous discovery of 11 new open cluster candidates within the lines of sight we analyzed. We present our technique, its advantages and challenges, as well as publish our membership lists and updated cluster parameters.

Keywords: Methods: data analysis – open clusters: general – astrometry

1. INTRODUCTION

Open clusters (OCs) are single stellar populations that formed together. Thousands of OCs have been identified and are widespread throughout the Milky Way disk (Friel 1995; Kharchenko et al. 2013; Dias et al. 2014). Studying OCs offers insights into theories of star formation (Kroupa 2001) and provides a direct view of the high mass end of the stellar initial mass function. OCs are also sites of few-body dynamical mechanisms that can produce unique astronomical objects such as Blue Straggler stars (Perets 2015; Toonen et al. 2020; He & Petrovich 2017). Taken as a whole, the OC population are key tracers of chemical enrichment throughout the Galactic disk (Spina et al. 2021).

³⁹ Identifying the members of a particular open cluster ⁴⁰ can be difficult and numerous techniques have been de-⁴¹ veloped to tackle the problem. Many techniques rely on ⁴² finding the population of stars in proper-motion space.

In proper-motion space, the population of stars that form an OC will appear as a compact group of similar proper-motions. This grouping can be identified straightforwardly for those open clusters whose propermotions are high enough that they are separate and distinct from the galactic field stars (e.g., Melotte 25 (the Hyades) in Figure 1, top-panel). However, more embedded OCs, such as Melotte 20 (see Figure 1, bottompanel), present a greater challenge.

With the advent of precise astrometric data from the Gaia survey (see Prusti et al. 2016; Brown et al. 2018), it is now possible to distinguish and computationally extract open clusters even when the kinematics of the cluster and field stars are not significantly different from one another. We briefly review some commonly employed methods here, but see Hunt & Reffert (2020) for a thorough and comprehensive review.

Cluster and cluster member identification algorithms
that use astrometric data leverage the compact nature of
calcuster in some combination of position, distance, and
proper motion. Most techniques employ what could be
called a 'bottom-up' approach in which the star cluster
bis built up out of smaller components until all the stars
within a line of sight are either considered a 'cluster'
star or a 'field' star.

Algorithms such as K-means (Utsunomiya et al. 1996), fit a K number of clusters to data by iteratively finding K mean centroids until some convergence threshold is met. Other algorithms, such as DBSCAN (Daszykowski & Walczak 2009), assign groupings of stars to clusters using inter-particle distance. One benefit of these algorithms is that they are not confined to proper-motion data, and have been successfully applied to position and multi-dimensional astrometric data (Gao 2018; Castro-Ginard et al. 2018). Both DBSCAN and K-means have been used to identify stars in known open clusters, but they have also been successfully employed to find new open cluster candidates (Cantat-Gaudin et al. 2019; Liu & Pang 2019; Castro-Ginard et al. 2019).

Despite its power and versatility, K-means algorithms 83 necessitate pre-defining the number of clusters that are 84 to be found. This may be difficult to do without explicit 85 prior knowledge of how the data are distributed along 86 the dimensions of interest. Workflows using K-means 87 also typically assume that the data are all distributed 88 spherically, a clear limitation when presented with more 89 realistic cluster shapes (Pang et al. 2021). DBSCAN is 90 more generalized than K-means in that it can find non-91 symmetric clusters distributed throughout the data, and 92 also doesn't require a preset number of clusters. How-93 ever, it becomes computationally expensive when con-94 sidering large data sets in more than 3 dimensions, as 95 all of the pairwise distances between data points must ₉₆ be calculated. The hyperparameters used in DBSCAN 97 to define clusters also needs to be fine-tuned, requiring 98 hyperparameter optimization which can become compu-99 tationally expensive.

Once OC candidates have been selected and preliminary membership is assigned, it is still necessary to ensure that the selected group of stars is a true physical cluster. One of the more reliable confirmation techniques for the overall cluster is to directly inspect the
candidates in color-magnitude space. A group of stars
with a narrow range of parallax can masquerade as a
cluster within a CMD. However, false cluster members
with erroneous parallax measurements will appear in unphysical locations within the CMD. Requiring member
stars to be clustered in proper-motion as well as distance also limits false-positive cluster identification. As

open clusters represent a single stellar population, the color-magnitude plot will exhibit well-known properties: the main sequence, the binary main sequence, and the red giant branch sequence if the cluster is sufficiently old. This technique becomes even more effective when previous values of the star cluster are known, such as metallicity ([Fe/H]), age, and extinction (A $_V$). A theoretical isochrone can then be generated to compare the observed colors and magnitudes of the stars with what would be expected from stellar evolutionary theory.

Perhaps the hardest aspect of such confirmation meth123 ods is that they are often performed manually for each
124 individual OC. This becomes a daunting task, consider125 ing that the Milky Way Star Cluster (MWSC) catalog
126 Kharchenko et al. (2013) contains over 2000 open clus127 ters.

There have been great strides in automating the pro-129 cess of open cluster membership construction to be able 130 to take a census of the Milky Way population.

Cantat-Gaudin et al. (2018a) recently performed one of the largest OC automated analyses in Gaia DR2, deriving mean cluster parameters (α , δ , $\mu_{\alpha*}$, μ_{δ} , ϖ , r_{core} , where the description as well as individual membership lists for 1229 OCs throughout the Milky Way. Cantat-Gaudin & Anders (2019) updated these results and grew their catalog to 137 1481 clusters.

Their method relies on finding all sub-clumps defined by running a K-means algorithm in their chosen sight lines. They then use the minimum spanning tree metric, Λ (Allison et al. 2009), to distinguish between concentrated star cluster sub-clumps and uniformly distributed sub-clumps of the same number that are found in the field. This was done iteratively to construct their final open clusters out of these sub-clumps. Finally, they produce membership probabilities by re-sampling the 3x3 covariance matrices of the stars and re-running their algorithm.

'Top-down' cluster identification algorithms, which aim to characterize the environment that includes the cluster, offer an alternative to the 'bottom-up' approach. Gaussian Mixture Models (GMMs) (Pearson 1893) describe a data set using a number of multivariate Gaussian components. GMM is a 'top-down' method that describes a line of sight (or subset thereof) as a mixture of multivariate gaussians. An individual gaussian, or component, of the model represents the cluster. GMMs have already been used to identify and characterize a number of astronomical objects, including individual open clusters (Gao 2018), the galaxy red sequence (Hao et al. 2009), and supernovae/host galaxy populations (Holoien et al. 2016).

215

GMMs allow for mixed memberships, wherein a data point can have a probability of belonging to multiple ple components. K-means and DBSCAN typically assumed sign each data point only to one component or cluster. GMMs also have fewer hyperparameters to tune than DBSCAN or other similar agglomerative clustering methods. The resulting covariance matrices from a well-fit GMM effectively describe the shape, scaling, and orientation of components within the data.

As Cabrera-Cano & Alfaro (1990) cautions in their analysis of ~ 300 stars in NGC-2420, care must be taken when fitting an OC dataset with GMMs. If the field star fraction is too large, the OC may be overwhelmed by field stars along the line of sight. An open cluster may be also be less separable if the distribution of field stars is strongly non-gaussian. Both of these situations may produce less than optimum results, although a quantitative analysis of the effect of these potential issues on a given cluster was not addressed.

It is ideal for a GMM to fit an intrinsic, underlying distribution rather than noisy discrete data. To accomplish this the observed measurements must first be deconvolved from their uncertainties Bovy et al. (2011) developed a method to determine the underlying distribution function in the presence of noisy data called Extreme Deconvolution'.

Extreme Deconvolution Gaussian Mixture Models (hereafter, XDGMM) combine the two techniques to ideally fit the true, intrinsic distribution with a gaussian mixture model. XDGMM has already been employed successfully to characterize members of a Galactic open cluster (Olivares et al. 2019) and to calculate mean cluster positions and proper-motions in the case of an actively disrupting open cluster (Price-Whelan et al. 2019). However, these use cases of XDGMM were for a small number of individual systems.

In this paper, we use XDGMM to identify members of known open clusters within Gaia DR2. We construct an automated pipeline to address the shortcomings of GMM cluster fitting – computational cost, the number of gaussian components to fit, and selection of the gaussian component associated with the cluster.

In Section 2 we discuss the Gaia DR2 data. In Section 3 we describe our method to extract open clusters. We present the mean cluster parameters and the properties of designated cluster members as well as a validation of our results via comparison with the literature in Section 4. In Section 5, we describe the serendipitous discovery ery of 11 new candidate open clusters not found in the current literature. Finally, we summarize our findings on open cluster extraction using an automated machine learning method and discuss future work in Section 6.

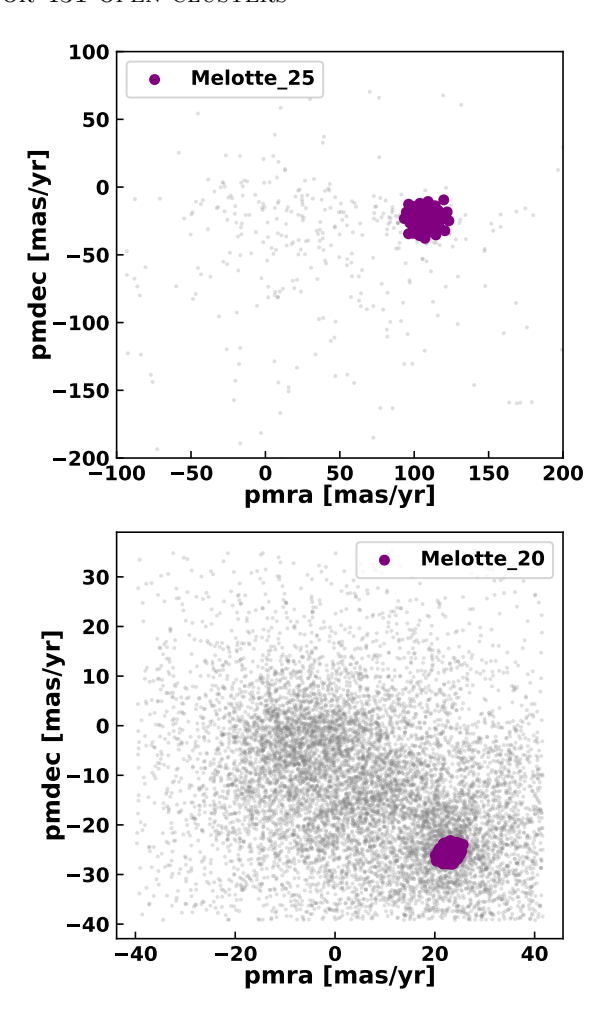


Figure 1. Proper-motion vector plot for Melotte-25, aka The Hyades Cluster (top panel, purple dots), and Melotte-20, aka the Alpha Persei Cluster (bottom panel, purple dots). Manually selecting open cluster members using vector point diagrams in proper-motion are easier (top panel) for some clusters than for more embedded clusters (bottom panel).

2. DATA

We first assemble a list of open clusters to conzir sider using the cluster catalog from Ahumada & Lazis passet (2007), originally created in their search for blue
zis straggler stars. They constructed a catalog of 427
ziz open clusters throughout the Milky Way, using Johnzi son UBV photometry (Johnson & Knuckles 1955) and
ziz isochrones (Girardi et al. 2000). We remove one known
zi asterism (NGC-1252 Kos et al. 2018; Angelo et al.
ziz 2019; Cantat-Gaudin & Anders 2019) from considerazis tion. This reduces the total number of open clusters we
zic consider to 426.

The effectiveness of any search for or characterization of open clusters will depend upon the input data. Gaia DR2 contains 5 dimensional astrometric measurements

₂₃₀ – position (α, δ) , proper motion $(\mu_{\alpha*}, \mu_{\delta})$, and paral- $_{231}$ lax (ϖ) – and photometry for over 1.3×10^9 sources 232 (Lindegren et al. 2018). The quality of this data set 233 makes it ideal for open cluster searches while its quan-234 tity presents a challenge. Attempting a global XDGMM 235 fit over the entire sky is computationally prohibitive and 236 would yield a suboptimal result even if possible (Sec-237 tion 3).

For each cluster, we define a target field of poten-238 239 tially associated Gaia DR2 sources. The target field 240 of view is centered on the position of the cluster and 241 has conservatively-wide opening angle to ensure that we do not remove potential cluster members and affect our subsequent analysis. While Ahumada & Lapasset 244 (2007) report both cluster positions and angular sizes, we supplement their measurements with the more re-246 cent open cluster catalog efforts of Dias et al. (2018) and ²⁴⁷ Kharchenko et al. (2013). The addition of these catalogs 248 and variation amongst them also captures the uncer-249 tainty of these input cluster parameters in our analysis. ²⁵⁰ Our target field center is the median of the positions ²⁵¹ reported in these cluster catalogs. The opening angle $_{252}$ is equal to $1.5\times$ the largest cluster angular diameter reported amongst Ahumada & Lapasset (2007), Dias et al. (2018), and Kharchenko et al. (2013).

We searched for all Gaia DR2 sources within the 426 255 256 target fields of view. We obtained the astrometric α , δ , ₂₅₇ $\mu_{\alpha*}, \mu_{\delta}, \varpi$ and photometric $[G, G_{BP}, G_{RP}]$ measure-258 ments, as well as the relevant uncertainties and corre-259 lation coefficients. In addition to the Gaia DR2 data, ²⁶⁰ we collected all previous distance determinations to the 261 clusters in our sample through the SIMBAD(Wenger et al. 262 2000) database. These distance measurements will be used in a pre-processing step described in Subsection 3.1. We used the ASTROQUERY python module (Ginsburg et al. 2019) to query both Gaia DR2 and SIMBAD.

3. METHODS

266

267

Ultimately, we identify a cluster and its members via a 268 XDGMM fit of the density field represented by standard-269 ized $\mu_{\alpha*}$, μ_{δ} , and ϖ measurements and uncertainties of 270 stars in the cluster vicinity. Our procedure's computational cost and its effectiveness correlates with the den-272 sity contrast between the cluster and field. We address 273 both of these concerns by first restricting each target 274 field to a manageable subsample.

The position information of the subsample of stars 275 associate with each cluster is only used for validation 277 purposes (Section 3.3.4). We make this decision based 278 on the work of Hillenbrand & Hartmann (1998), Kuhn 279 et al. (2014), and Kuhn et al. (2017). These works con-280 sidered clustering of star clusters using their observed

281 on-sky positions. They found that a multivariate normal 282 distribution may not be best fit to these distributions.

We scale the measurements and uncertainties of inter-284 est to account for the different variance of each feature 285 before applying the XDGMM fit. Finally, we establish 286 quantitative metrics to select the number of components 287 to include in the XDGMM fit and to select the individ-288 ual component corresponding to the cluster. The details 289 of our method follow.

3.1. Data Preprocessing

290

The Gaia DR2 data is known to have systematics that, 291 292 if unaccounted for, can lead to erroneous or biased re-²⁹³ sults (Vasiliev 2019). We use the recommendations from ²⁹⁴ Lindegren et al. (2018) to account for systematics found 295 within the parallax and proper-motion data. In par-296 ticular, we subtract the -0.029 mas parallax zero-point 297 from all of our stars and exclude all stars fainter than 298 18th Gaia G magnitude. Our faint limit reduces the to-299 tal number of stars included in our analysis. Stars with $m_{\rm G} > 18$ typically have high fractional astrometric un-301 certaines in Gaia DR2 making them ill-suited for cluster-302 finding (e.g. Cantat-Gaudin & Anders 2019; Hunt & Ref-303 fert 2020). We also correct for the inertial spin found 304 within the proper-motions of bright sources using the 305 recommendations from Lindegren (2019).

After applying the global corrections and limits, we 307 preprocess the input data within each cluster target field 308 independently. The goal is to remove obvious field stars 309 and astrometric outliers from consideration as cluster 310 members. This reduces the dynamic range of parallax and proper motion and, in turn, increases the signal of 312 any over-density associated with the cluster.

We first remove outlier stars in proper motion. Stars with $\mu_{\alpha*}$ or μ_{δ} measurements more than 10σ away from 315 the median of their target are dropped from considera-316 tion. Individual high proper-motion stars may skew the 317 feature scaling within a target field. This step is per-318 formed for all clusters except for the high proper-motion 319 cluster Melotte-25 (the Hyades cluster).

We remove parallax outliers only if more than 10^4 321 stars in a target field remain eligible for XDGMM fit-322 ting. We found that this numerical threshold strikes a 323 good balance between ensuring a complete cluster mem-324 bership list given our magnitude limit and maintaining 325 computational efficiency of the XDGMM fitting. If a $_{326}$ target sample contains $> 10^4$ stars, we discard the stars 327 least likely to be at the distance of the known cluster.

The open clusters have uncertain literature distances 329 and there is uncertainty measured parallax of each star.

 $^{^1}$ Gaia DR2 $G<11\,$

330 For these reasons, we do not simply discard stars using a 331 strict delta parallax cut-off. Rather, we employ a simple 332 probabilistic model to determine the stars least likely to 333 be within the literature parallax range of the cluster.

We assume the parallax of cluster members is distributed normally with a mean μ and standard deviation 336 σ given by:

$$\mu = med(arpi_{lit}),$$

 $\sigma = \begin{cases} 0.25 \cdot med(\varpi_{lit}) , & \text{if } med(\varpi_{lit}) > 1 \text{ } mas \\ 0.25 \text{ } mas, & \text{if } med(\varpi_{lit}) < 1 \text{ } mas \end{cases}$ (1) where $med(\varpi_{lit})$ is the median of the cluster par-

339 allaxes reported in the three cluster catalogs sources

340 we examine (Section 2). We set σ to depend on $med(\varpi_{lit})$. Clusters with a literature parallax less than $_{342}$ 1 mas (distance greater than 1 kpc) have a constant σ_{ϖ} 343 of 0.25 mas. Clusters with a literature parallax greater than 1 mas have their σ_{ϖ} set to a 25% of their median 345 literature parallax. This ensures that the parallax dis-346 tribution of nearby clusters is not excessively truncated. We use bootstrap sampling to calculate the proba-348 bility that each stellar parallax measurement is drawn 349 from the cluster parallax distribution. For each star, we 350 sample a normal distribution with mean $\mu = \varpi_{obs}$ (gaiadr2.parallax) and $\sigma = \sigma_{\varpi_{obs}}$ (gaiadr2.parallax_error) 352 1000 times. We then evaluate the PDF of the corresponding cluster, defined in equation 1, at the locations of these 1000 samples. The star's probability of parallax overlap is then the mean of the 1000 PDF evaluations. Only the 10^4 stars with the highest parallax overlap probability within the target field are kept and subject 358 to XDGMM fitting. After this step, all target fields have been reduced to a maximum of 10^4 stars based on 360 the closeness of their parallax and proper motion to the 361 parent cluster. All of the analysis and XDGMM fit pro-

3.2. Scaling the $\mu_{\alpha*}$, μ_{δ} , ϖ data

cedure described below pertain only to these restricted

363 data.

Feature scaling is necessary to establish an appropri-366 ate shape of the parameter space as we are fitting 3-367 dimensional data with unequal means and variance. We 368 use 'StandardScaler' from the Scikitlearn (Pedregosa 369 et al. 2015) python package, which shifts and scales the 370 data in each to dimension to a mean of zero and a variance of one.

We first smooth the data before scaling to ensure 373 we calculate the scaling parameters accurately. The smoothed distribution is a simple resampling of the $[\mu_{\alpha*}]$, $_{375}$ μ_{δ} , ϖ distribution according to the uncertainty co-376 variance matrix (equation 2). We resample each star

 $N_{samples}$ times such that StandardScaler uses approx-378 imately 5×10^4 coordinate positions (i.e., $N_{samples} \times$ $N_{data} = \sim 5 \times 10^4$, where N_{data} is the number of stars 380 remaining in the field after pre-processing). The shift 381 and scale parameters found for the smooth distribution are then applied to the actual measurements prior to fit-383 ting. We scale the measurement uncertainties as well, to 384 preserve the fractional uncertainty of each measurement 385 in the transformed data space.

3.3. XDGMM fit of the scaled data

Gaussian Mixture Models employ the assumption 388 that any N-dimensional data can be represented as the 389 summation of K components, each of which is an N-390 dimensional Gaussian. The K Gaussian distributions 391 have K means, and K covariances.

XDGMM takes into full account the full covariance matrix representing the uncertainty on $\mu_{\alpha*}$, μ_{δ} , and ϖ , 394 and the correlation ρ for each data point. This covariance matrix is assembled as written in equation 2.

$$\begin{pmatrix} \sigma_{\mu_{\alpha*}}^{2} & \sigma_{\mu_{\alpha*}}\sigma_{\mu_{\delta}}\rho_{\mu_{\alpha}\mu_{\delta}} & \sigma_{\mu_{\alpha*}}\sigma_{\varpi}\rho_{\varpi}\mu_{\alpha*} \\ \sigma_{\mu_{\delta}}\sigma_{\mu_{\alpha*}}\rho_{\mu_{\alpha}\mu_{\delta}} & \sigma_{\mu_{\delta}}^{2} & \sigma_{\mu_{\delta}}\sigma_{\varpi}\rho_{\varpi}\mu_{\delta} \\ \sigma_{\varpi}\sigma_{\mu_{\alpha*}}\rho_{\varpi}\mu_{\alpha*} & \sigma_{\varpi}\sigma_{\mu_{\delta}}\rho_{\varpi}\mu_{\delta} & \sigma_{\varpi}^{2} \end{pmatrix}$$
(2)

We perform an XDGMM fit of the scaled astrometric 398 data and the associated scaled covariance matrices us-399 ing the XDGMM python wrapper (Holoien et al. 2016). 400 Each cluster target field is fit independently.

3.3.1. Determining the number of XDGMM components

We fit each cluster-specific scaled data set nine times, 403 using from 2 to 10 Gaussian components. We do not 404 fit more than 10 components due to the computational 405 cost. All model fits converge within a tolerance of 1 \times $406 \ 10^{-8}$ and use a random seed of 999.

Of the nine XDGMM fits to a cluster, we select the 408 best-fit model according to the Bayesian Information 409 Criterion (BIC Ghosh, Jayanta K. et al. 2006). The 410 BIC is commonly used to select between models when 411 fitting to a data set as it strikes a balance between maxi-412 mizing the likelihood and penalizing the introduction of ⁴¹³ new parameters to avoid over-fitting. The BIC is defined 414 as,

$$BIC = x \cdot \log n - \log \hat{L}, \tag{3}$$

416 where x is the number of parameters needed in the 417 XDGMM fit, n is the number of data points, and \tilde{L}

418 is the maximized likelihood of the model. The best-fit 419 model has the lowest BIC score.

We find that the optimal number of components in the best-fit model is typically between 5 and 8 and correlates with the number of stars in the target field (Figure 3). Heavily populated target fields (>5000 stars; black dashed histogram) generally required more components in the best-fit model than sparsely populated fields (red histogram).

3.3.2. Finding the Open Cluster component

427

435

456

We use the differential entropy information metric to select the gaussian component that best describes the open cluster. Differential entropy is a measure of how compact a distribution is within a volume. In this case, we can ascertain the compactness of each gaussian component in the scaled data space. For a multivariate gaussian, the differential entropy (h) can be written as,

$$h = \frac{d}{2} + \frac{d}{2}ln(2\pi) + \frac{1}{2}ln(|\Sigma|),$$
 (4)

where d is the dimension of the parameter space and $|\Sigma|$ is the determinant of the covariance matrix for the multivariate gaussian of each component in the best-fit XDGMM (see Ahmed & Gokhale 1989).

We automatically designate the component with the lowest differential entropy as the cluster component.

3.3.3. Individual membership probabilities

Once we have determined the optimal number of components and which component belongs to the open cluster, we employ bootstrap resampling to calculate the open cluster membership probabilities of each star in the scaled target field. We assign each star within a target field to a component using the XDGMM code's built-in 'predict' function. We then generate a new scaled $[\varpi, \mu_{\alpha*}, \mu_{\delta}]$ value for each star from its scaled 3x3 covariance matrix. We recompute component assignments for each star for a total of 100 iterations. The final membership probability of any one star is the number of times that the star was assigned to the open cluster component out of 100.

3.3.4. Validation of fit results

We visually inspect the resulting open cluster model results by plotting four different characteristics of the cluster stars with a membership probability above 50%. We plot the proper-motion of the stars in α and δ the G and G_{BP} - G_{RP} color-magnitude diagrams, the positions in l and b, and ϖ as a function of G-band magnitude. We show these four panels for the cluster NGC-6583 in Figure 2 as an example.

We define a successful open cluster retrival, in the broadest sense, via visual validation. Statistical tests can be found in Section 4. We retrieve a known open cluster when the resulting members (probability >50%) are concentrated in proper-motion vector space, form a relatively well-defined isochronal color-magnitude sequence, are centered within the target field on-sky, and occupy a narrow distribution in parallax as a function of G-band magnitude.

4. RESULTS

474

We successfully recover 420 of the 426 known open clusters targeted. The probable members of these identified clusters are highly concentrated in proper-motion and parallax space relative to field stars and populate a narrow isochrone in the color-magnitude diagram (Section 3.3.4). We statistically validate our cluster membership designations and the astrometic location of the recovered clusters in Section 4.2.

Our automated pipeline to select the best-fit XDGMM 484 and identify the individual Gaussian component corre-485 sponding to the cluster target required no human in-486 tervention in 95% of the investigated target fields. In 487 these 385 fields, the lowest differential entropy (h) com-488 ponent of the best-fit model represented the targeted 489 cluster. The remaining 41 fields required manual analy-490 sis of XDGMM fits. We found the target cluster was fit 491 by the second lowest h component of the best-fit model 492 in 29 of the manual analysis fields. In nearly all (28/29) 493 of these target fields, the minimum h component was 494 either a spatially adjacent known open cluster or a new 495 open cluster candidate (Section 5). All told, the min-496 imum h component of the best-fit XDGMM identified ⁴⁹⁷ a cluster or candidate cluster in 413 of the 426 target 498 fields.

None of the best-fit model components fit describe the known cluster in remaining 12 target fields. We visually inspected all 54 ($\sum_{i=2}^{10}i$) components within the 9 BIC-scored model fits to each of these target fields in search of a component that corresponded to the known open cluster. We identified a Gaussian component that represented the open cluster in 6 of these target fields.

In the remaining 6 target fields, we were unable to recover a cluster candidate component either automatically or manually despite convergence of the XDGMM code. At least 2 of these 6 targeted clusters likely violate our assumption of the open cluster being a significant over-density in the $[\mu_{\alpha*}, \mu_{\delta}, \varpi]$ space. Ruprecht-46 may be an asterism masquerading as a cluster, as was recently argued by Cantat-Gaudin et al. (2020). Collinder- 228 is a well-known cluster in the Carina Nebula, but Feigelson et al. (2011) found that the cluster is a com-

591

⁵¹⁶ position of many sparse groups with no clear central ⁵¹⁷ concentration.

Nevertheless, our automated pipeline was successful in a variety of conditions. Within the 385 target fields with a fully automated and successful target cluster recovery:

521

522

523

524

525

526

527

- 1. The target field contains a total number of stars as few as 123 stars and as many as 1×10^4 stars
- 2. The number of cluster member stars (with a membership probability > 0.5) was as few as 40 stars and as many as ~ 3700 stars
- 3. Cluster members comprised a wide range, 0.64% 54.5%, of all stars in the target field

This work is, to the best of our understanding, the first to report central parameters using Gaia DR2 for some of the target clusters. We identify 11 clusters that are not included in the Gaia DR2 based cluster catalogs of Cantat-Gaudin et al. (2018a), Cantat-Gaudin et al. (2019), Castro-Ginard et al. (2018), Castro-Ginard et al. (2019) Castro-Ginard et al. (2020), Ferreira et al. (2020), Sim et al. (2019), Liu (2019), or Hunt & Reffert (2020). Cluster parameters for these systems can be found in Table 1.

Our cluster member catalog contains 261 662 stars with non-zero membership probability ($P_{\rm mem}$). In our subsequent analysis, we define members, probable members, and highly probable members of a cluster as those stars with $P_{\rm mem}$ greater than 0.5, 0.85, and 0.95, respectively.

The member catalog of the 420 recovered open clusters includes 171 939 cluster members, 125 235 probable members, and 95 920 highly probable members. We list 10 entries for 10 cluster members and their Gaia DR2 measurements in Table 2.

Finally, we report the serendipitous recovery of several candidate open clusters. The XDGMM component corresponding to the candidate clusters had low differential entropy and the properties of the candidate members are consistent with open clusters. These candidates were discovered within the 426 target fields but are not found in the Ahumada & Lapasset (2007) catalog. We describe our method for identifying these open cluster candidates and their properties in Section 5.

4.1. Cluster Astrometric Parameters and Distances

We determine robust central astrometric coordinates $[\alpha, \delta, \varpi, \mu_{\alpha*}, \mu_{\delta}]$ of each cluster using the measurements of probable members (Table 1).

To do so, we first remove potential outlier measurements via a sigma-clipping procedure. We calculate an initial coordinate median and median absolute deviation $_{565}$ (MAD), both weighted by inverse measurement uncer- $_{566}$ tainty, of probable members. We estimate σ assuming $_{567}$ a normal distribution using $\hat{\sigma}=1.4826\times \text{MAD}$ (e.g., $_{568}$ Huber 1980). We discard all outlier measurements not $_{569}$ within $\pm 3~\sigma$ of the initial weighted median.

We then recalculate the weighted median and MAD of the non-outlier stars for each of the 5 astrometric parameters. We list these median values and the standard deviation estimator $\hat{\sigma}$ in Table 1. We also calculate the radius, containing half of the cluster members, using the cluster positions and list these values in 1.

Cluster distance, while not a direct astrometric measurement, can be ascertained to a relatively high precision because each cluster member can be assumed to lie at nearly the same distance along the line of sight. Simple parallax inversion is not adequate to measure physical distances using Gaia DR2. This is due to the nature of the Gaia DR2 parallax measurements which may be close to zero or even negative. We obtain individual cluster distances through Bayesian Inference (see Luri et al. 2018, for more details).

The posterior probability of the cluster distance can be expressed as,

$$P(r|\{\varpi\}, \{\sigma_{\varpi}\}, L) \propto P(r|L)P(\{\varpi\}|r, \{\sigma_{\varpi}\}), \quad (5)$$

where P(r|L) is the exponential decreasing space density prior (Bailer-Jones 2015):

$$P(r|L) = \begin{cases} \frac{1}{2L^3} r^2 e^{-r/L}, & \text{if } r > 0\\ 0, & \text{otherwise} \end{cases}$$
 (6)

and $P(\{\varpi\}|r, \{\sigma_\varpi\})$ is the likelihood of observing the set of parallax measurements given a true cluster distance r and the set of measurement uncertainties and is given by,

$$P(\{\varpi\}|r, \{\sigma_{\varpi}\}) = \prod_{i=1} \frac{1}{\sqrt{2\pi\sigma_{\varpi_i}^2}} exp\left(-\frac{(\varpi_i - \frac{1}{r})^2}{2\sigma_{\varpi_i}^2}\right).$$
(7

We set the length scale 'L' within our prior to be 1 $_{598}$ kpc and compute the posterior over a distance range of $_{599}$ [0.01, 30] kpc.

We sample the posterior distribution and compute the 16^{th} , 50^{th} , and 84^{th} percentile distances for all 420 open clusters and the open cluster candidates (Section 5). Table 1 contains our distance measurements to the 11 newly confirmed open clusters in Gaia DR2 and our 11 new open cluster candidates. The full table of all 420 open clusters mean astrometric parameters and inferred distances will be made available electronically.

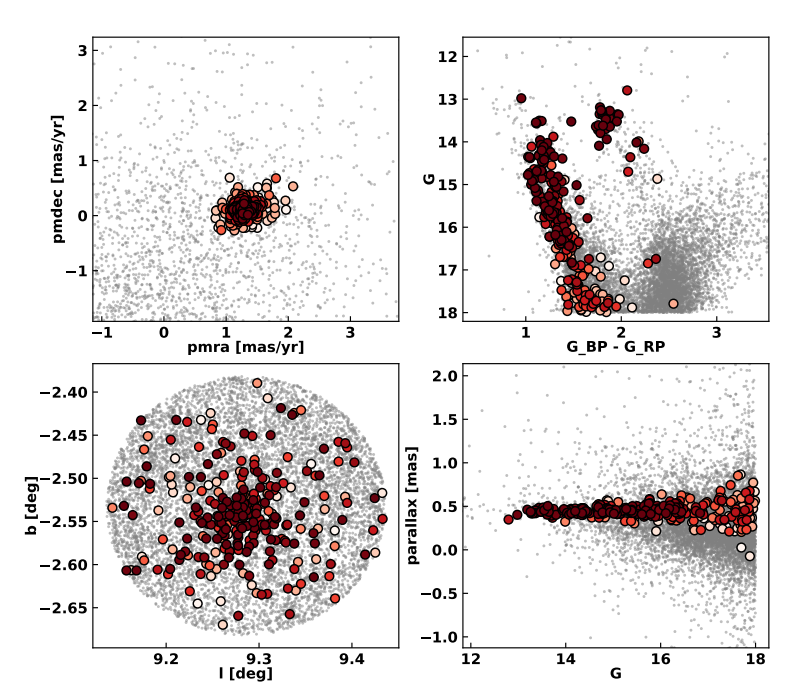


Figure 2. An example four panel plot used for visual validation of a fully automatic XDGMM extraction. The open cluster is NGC-6583. In all four panels, the field is given by gray dots, and the cluster stars are given by the red circles, where the lower membership probability stars tend towards white in color. The top left panel is a vector point diagram plot in proper motion. The top right panel is a color-magnitude diagram using Gaia filters. The bottom left panel is a plot of positions in galactic coordinates. The bottom right panel is a plot of the parallax measurements for cluster stars as a function of their Gaia G-band magnitude.

We acknowledge that the range between the 16^{th} and 84^{th} distance percentiles may be artificially narrow. Equation 7 implicitly assumes that all cluster members reside at a singular distance rather than occupy a small, realistic range in distance along the line of sight. The assumption greatly simplifies the calculation and is relatively accurate for distant clusters. However, our treatment may not be the most suitable for very nearby open clusters such as Melotte-25 (the Hyades, $\varpi \sim 21 \text{mas}$), and Melotte-22 (the Pleiades, $\varpi \sim 7 \text{mas}$).

4.2. Verification of our catalog results

618

To ascertain some measure of the veracity of our results, we first compare our central cluster parameters and membership lists to previously published membersize ship catalogs.

In addition, we use the more recent Gaia eDR3 data (Brown et al. 2020) to determine if the cluster members unique to this work are actual cluster stars or field contamination.

4.2.1. Comparison with previous results in the literature

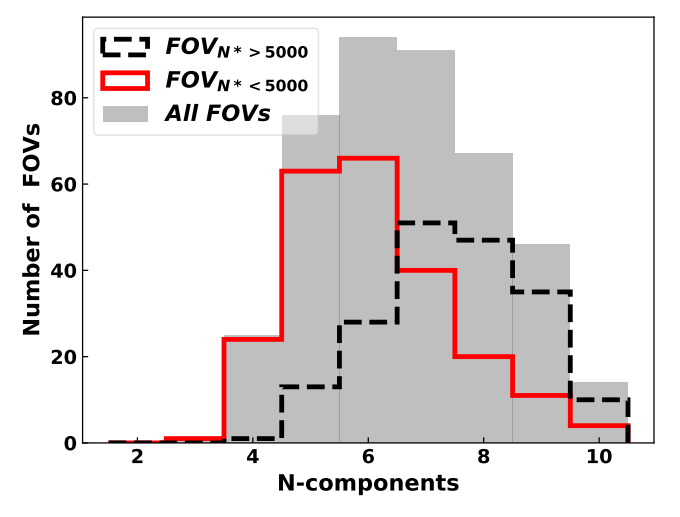


Figure 3. Histogram of the number of components selected successfully with the BIC for 414 target field XDGMM fits. The complete distribution is given by the gray shaded histogram. The red solid line is the distribution of the number of components for all target fields with less than 5000 stars. The dashed black line is the distribution of the number of components for all target fields with more than 5000 stars. We find that the more populated target fields required more components to disentangle the open cluster from the field than sparser target fields.

We can further scrutinize our results by comparing the mean cluster parameters for our sample with those clus-629 mean cluster parameters for our sample with those clus-630 ters which have entries within the literature. We plot 631 the empirical cumulative distribution functions(eCDF) 632 of the residuals between each cluster's parameter cal-633 culated in this work with the literature parameters in 634 Figure 4.

The difference in ϖ , $\mu_{\alpha*}$, and μ_{δ} was computed for 392 clusters this work has in common with Cantat-Gaudin et al. (2020). We find that the difference in ϖ , $\mu_{\alpha*}$, and μ_{δ} is quite small, with median values of 0.031 mas, -0.002 mas yr⁻¹, and 0.004 mas yr⁻¹, respectively. The offset of 0.031 mas in the ϖ appears to come from our application of the -0.029 mas zero-point offset (see Section 3.1). Removing this zero-point offset from the cluster ϖ values leads to a median difference of only 0.002 mas with the literature values. This level of agreement with a study using a completely different cluster identification algorithm is strong evidence that we successfully recover the central location of our target clusters.

We find good agreement between our inferred clus-649 ter distances and those from Cantat-Gaudin & Anders 650 (2019). The median difference in distance is -0.003651 kpc. The range between the 84^{th} and 16^{th} percentiles 652 in the distance discrepancy is only 0.036 kpc.

We also find good agreement in r50, the radius containing half the cluster members. The median difference in r50 between the results of Cantat-Gaudin & Anders (2019) and our own is 0.003 deg. We do report much smaller r50 values for about 10% of clusters (Figure 4, bottom left, x <-0.10 deg). Upon investigation, we find that these clusters, according to Cantat-Gaudin et al. (2020), extend beyond the aperture radius employed in this work to define the input target field (Section 2). Thus, the cluster members recovered in this work may populate as wide a range in position for the clusters with large angular sizes. However, based on the agreement in cluster mean ϖ , $\mu_{\alpha*}$, and μ_{δ} , this does not appear to affect our ability to recover the bulk of the clusters in question.

The general agreement in cluster mean parameters suggests that our cluster member lists have significant overlap with those of Cantat-Gaudin et al. (2020). We compare our catalog with the catalog of Cantat-Gaudin et al. (2020) using Gaia DR2 source ids at a membership probability of > 25%, > 50%, and > 95%. We correct the aperture size to match our target field aperture.

At the lowest level of membership probability we find our that our cluster member list contains 98.7% of the members reported by Cantat-Gaudin et al. (2020) at the same membership probability according to their method. This overlap decreases to 96.1% at the next membership level. The overlap decreases to 81.1% at the highest level of membership.

The overlap in cluster members is a strong argument that our cluster member designation is largely accurate, since our method to construct the cluster membership lists differs from that of Cantat-Gaudin et al. (2020). The alternative, that our discrepant methods share the same false positives, appears unlikely.

We find that member stars in our catalog that are not found in Cantat-Gaudin et al. (2020) are fainter than the member stars shared in common between our two catalogs. The median Gaia DR2 G-band magnitude of common member stars with $P_{\rm mem} > 50\%$ is 15.67. The unique member stars found in this work have a median Gaia DR2 G-band magnitude of 16.77, a difference of 1.1 magnitudes. At $P_{\rm mem} > 95\%$, the median Gaia G-band of unique member stars identified in this work is still 0.6 magnitudes fainter than the highly probable members common to both catalogs. This could indicate that the XDGMM fit is more sensitive to the fainter stars in each target field, given the full treatment of each star's individual covariance matrix.

⁰² 4.2.2. Hertzsprung-Russell Diagrams of our Open Clusters

Open clusters populate isochrones within the Hertzsprung-Russell Diagram (HRD). The HRD is a well-known figure that relates a star's evolutionary state

706 to its color and absolute magnitude, in lieu of temper-707 ature and luminosity measurements, respectively. We 708 can check the reliability of our method of selecting open 709 cluster groups by placing them on the HRD and check-710 ing to see the bulk population properties of our member 711 catalog.

We calculate the absolute magnitudes of each cluster star prior to placing it on the HRD. The majority of the open clusters considered in this work reside within the galactic disk of the Milky way, occupying the galactic latitude (b) range [-20,20]. We need to correct for reddening and extinction due to galactic dust, as well as distance, to be able to place the cluster member stars on the HRD accurately.

Dust extinction and distance has already measured for 392 clusters in our recovered sample of 420 (93.3%) by Cantat-Gaudin et al. (2020). In Cantat-Gaudin et al. (2020) a neural network was developed and trained on CMDs of synthetic clusters constructed from 347 real cluster parameters in the literature, the bulk of which came from Bossini et al. (2019).

We use the polynomial fit equations of Babusiaux 728 et al. (2018) to determine the Gaia DR2 passband ex-729 tinction values, A_G , A_{BP} , A_{RP} for all stars in the 392 $_{730}$ clusters with A_V measurements from Cantat-Gaudin 731 et al. (2020). However, some stars have poor photometry 732 such that the Gaia extinction coefficients could not be 733 calculated. We circumvent this by selecting a high qual-734 ity sample of stars from each cluster. We select the stars $_{735}$ within each cluster with a probability > 0.85. We also $_{736}$ exclude all stars with $gaiadr2.phot_bp_rp_excess_factor$ $_{737} > 1.5 + 0.03 \cdot (G_{BP} - G_{RP})^2$ as this is indicative of large 738 systematic errors within the G_{BP} and G_{RP} colors (Riello 739 et al. 2018). The median A_G , A_{BP} , A_{RP} values of these 740 high quality cluster stars is then used to de-extinct and 741 de-redden stars all other stars in each cluster. This ap-742 proach allows us to apply dust corrections to all proba-743 ble cluster members, even those with more problematic 744 photometry. However, this means we do not account for 745 differential reddening present in very distant or heavily 746 extincted open clusters.

We plot the extinction-corrected absolute G band magnitude as well as the de-reddened G_{BP} - G_{RP} color of cluster members in Figure 5. We plot the HRDs that stars with membership probabilities greater than following greater than 85% (middle panel), and greater than 95% (right panel). We also color code the stars by their parent cluster age as predicted in Cantat-Gaudin et al. (2020).

Our HRD contains various groups at different stages 756 of stellar evolution, such as the main-sequence, main-757 sequence turn off, and red-giant branch. All of these

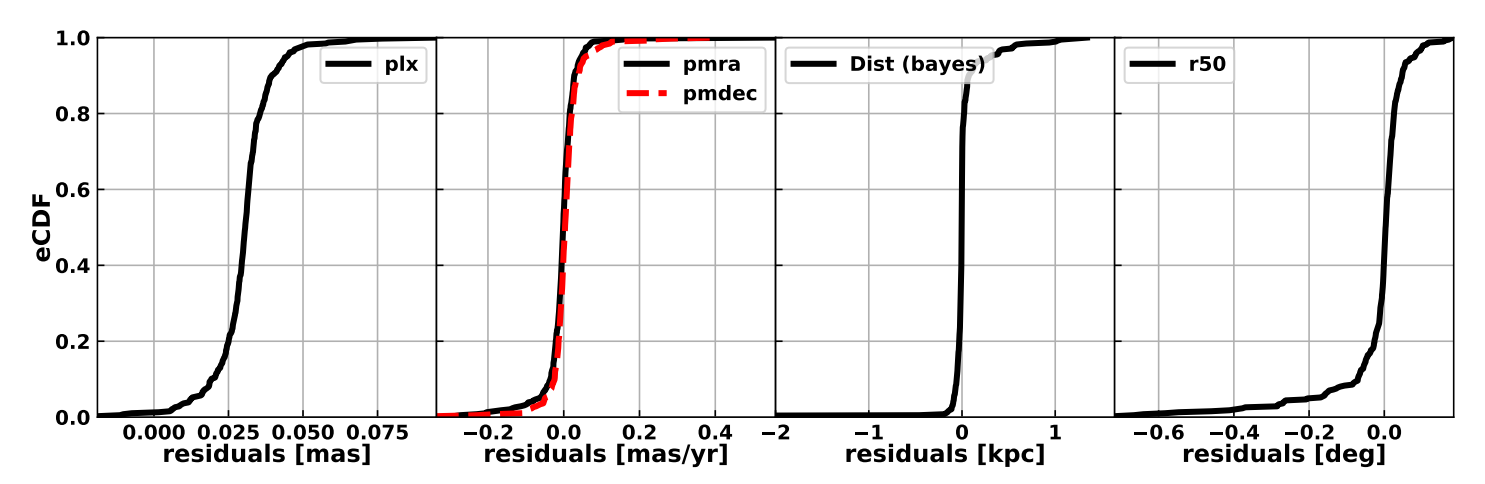


Figure 4. (In order from left to right) Comparison empirical cumulative distribution (eCDF) plots of the mean cluster ϖ , $\mu_{\alpha*}$ (black solid line) and μ_{δ} (red dashed line), distance from Bayesian inference (black solid line), and on-sky size containing half of all cluster members (r50). The ϖ , $\mu_{\alpha*}$, μ_{δ} , distance from Bayesian inference, and r50 eCDF plots are comparing the 386 clusters this work has in common with Cantat-Gaudin & Anders (2019). There is overall excellent agreement between mean open cluster parameters in our catalog with the values in the literature from different methods.

features are clearly visible even at the 50% membership probability threshold (Figure 5, left panel). We also refootover 12 white dwarfs as high probability cluster memfootover with this application of XDGMM. 5 are apparent members of the Beehive cluster (NGC-2632), 3 are in the
Hyades cluster (Melotte-25) while the Coma star cluster
footometer (Melotte-111), the Pleiades (Melotte-22), Graff's cluster
footometer (IC-4756), and the Pincushion cluster (NGC-3532) each
footometer have 1 white dwarf.

The overwhelming majority of the cluster member forms stars appear in physically sensible regions of the HRD. While it is true that a group of stars sharing the same parallax will form a diagonal sequence within the HRD, for our general and close agreement with the mean cluster parameters of previous studies (Section 4.2.1) is good evidence that we do not claim to find a known cluster at an incorrect astrometric position. Instead, the lack for stars at unphysical locations in the diagram, even at form the diagram, even at form to does not suffer from significant field contamination due to erroneous or uncertain parallax measurements. Stars with intrinsic parallax different from the target cluster would appear above or below the main locus.

The clear age gradient and features in the HRD offer more evidence that our cluster member designations are largely accurate. The main sequence turn-off in older clusters in clearly more red and dim than in younger clusters. If we erroneously labeled all stars near the cluster parallax as cluster members, the correlation between cluster age and turn-off position may have been weakened by field interlopers. In addition, we only find stars along the pre-main-sequence in the youngest clusters. The age labels of each cluster are taken from

791 Cantat-Gaudin et al. (2020), who use an entirely dif-792 ferent method of determining cluster membership. The 793 cluster ages shown in Figure 5 are completely decou-794 pled from our cluster membership designations, yet the 795 age-dependent features above remain.

Our cluster membership probabilities are calculated independent of any photometry, but we find a correlation between membership probability and position on the HRD relative to the expected locations predicted by cluster isochrones. A small percentage of stars appear between the main sequence and white dwarfs; others are redder than the red giant branch. These outliers are far less prominent in the $P_{\rm mem}>95\%$ panel. This correlation is clearly apparent for stars just below the main sequence $(G_{BP}-G_{RP}\approx 1 \text{ and } G\approx 7.5; G_{BP}-G_{RP}\approx 0 \text{ and } G\approx 2.5)$, colder than the main sequence turnoff, and with intermediate colors relative to the red clump and upper main sequence.

4.2.3. Membership Testing with Gaia eDR3

Gaia eDR3 (Brown et al. 2020) yields an opportunity to validate our cluster membership lists. The Gaia eDR3 astrometric data is nominally at higher precision than Gaia DR2 and can serve as a check on the quality of our cluster stars memberships. Specifically, we can statistically test for cluster membership by comparing the Gaia DR2 and eDR3 parallax measurements of the same star.

We first assume that the observed parallax does not suffer from systematic uncertainty nor bias and is normally distributed about the true parallax in both Gaia

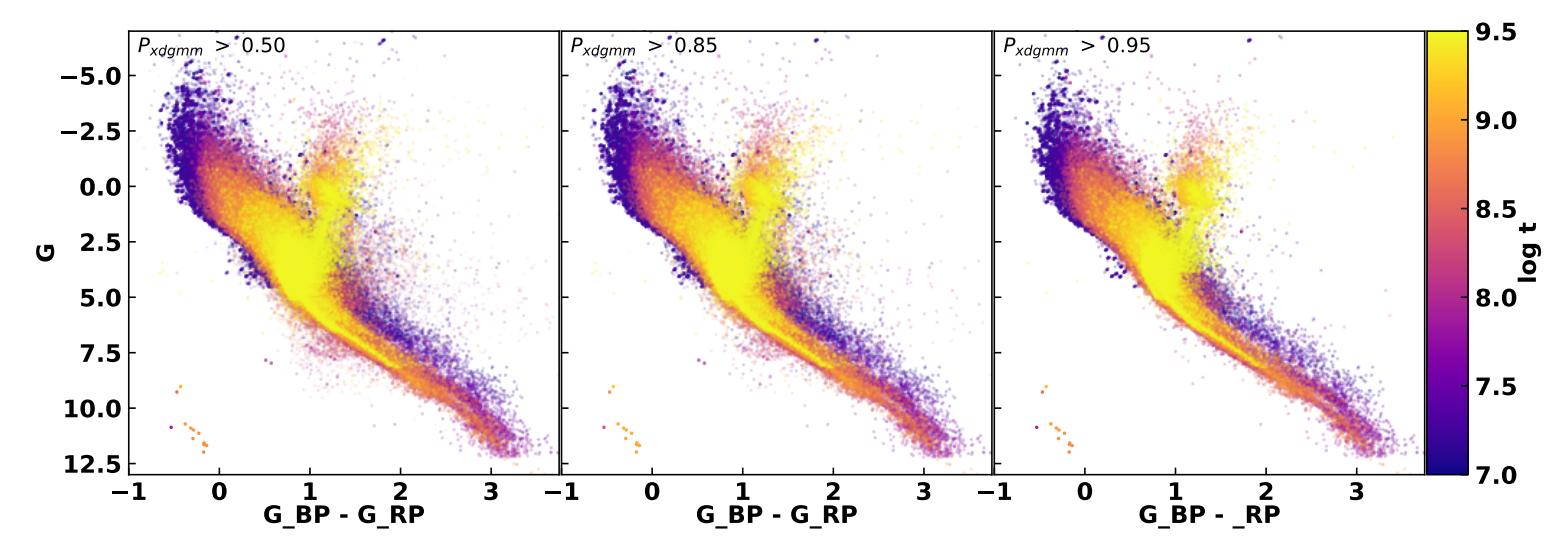


Figure 5. Hertzsprung - Russell diagram of all member stars within the 392 open clusters recovered in this work that also have predicted ages, extinctions, and distances in Cantat-Gaudin et al. (2020). All stars plotted have a G_{BP} - G_{RP} excess factor less than $1.5+0.03\cdot(G_{BP}-G_{RP})^2$. Stars with at least a 0.25 membership probability are plotted in the left panel, the 0.50 membership level stars are plotted in the middle panel, and the 0.95 membership level The stars are plotted in the right panel. The three Gaia passbands (G, G_{BP}, G_{RP}) have been corrected for extinction and reddening using the methods described in Babusiaux et al. (2018). We find that our use of XDGMM is able to properly capture multiple phases of open cluster evolution with no apparent biases.

820 eDR3 and DR2. The observed parallax in either data release is then (as in Luri et al. 2018),

$$p(\varpi_j|\varpi_{\mathrm{true}}) \propto \mathcal{N}(\varpi_{\mathrm{true}}, \sigma_{\varpi_j})$$
 (8)

where the subscript $j \in [DR2, eDR3]$ refers to the specific data release, ϖ_{true} is the true parallax of the star, $\mathcal{N}(\mu, \sigma^2)$ represents a normal distribution with mean μ and variance σ^2 , and σ_{ϖ_j} is the uncertainty of the parallax measurement in each data release.

The relationship between the parallax measurements in both Gaia data sets and the parallax (distance) of the cluster will be different for cluster and field stars. The true distance of a cluster corresponds to a singular cluster parallax, $1/d_{\rm clus} = \varpi_{\rm clus}$, if we ignore the small intrinsic width of the cluster. The observed parallax of a star relative to the cluster parallax is simply $\delta_{\varpi_j} = \varpi_j - \varpi_{\rm clus}$, where j again identifies the specific Gaia data release. For a bonafide cluster member, $\varpi_{\rm true} = \varpi_{\rm clus}$ and thus one expects the eDR3 parallax measurement to be closer to the true cluster parallax; i.e., $|\delta_{\varpi_{\rm eDR3}}| < |\delta_{\varpi_{\rm DR2}}|$ if $\sigma_{\varpi_{\rm eDR3}} < \sigma_{\varpi_{\rm DR2}}$. However, $\varpi_{\rm true} \neq \varpi_{\rm clus}$ for field stars in which case we expect $|\delta_{\varpi_{\rm eDR3}}| \sim |\delta_{\varpi_{\rm DR2}}|$.

The difference between Gaia eDR3 and DR2 measurements of the observed parallax relative to the cluster parallax, $\delta_{\varpi_{\rm eDR3}} - \delta_{\varpi_{\rm DR2}}$ should therefore be different for cluster and field stars. We define this change in relative

tive parallax $\Delta \varpi$ for a single star in terms of the relative Gaia DR2 parallax measurement as,

$$\Delta \varpi = \delta \varpi_{\text{eDR3}} - \delta \varpi_{\text{DR2}}$$

$$= \varpi_{\text{eDR3}} - \varpi_{\text{DR2}}$$

$$= \mathcal{N}(0, 1) \sigma_{\varpi_{\text{eDR3}}} - \mathcal{N}(0, 1) \sigma_{\varpi_{\text{DR2}}}$$

$$= \mathcal{N}(0, 1) \sigma_{\varpi_{\text{eDR3}}} - (\delta \varpi_{\text{DR2}} - \varpi_{\text{true}} + \varpi_{\text{clus}})$$
(9)

where the final two equalities make use of $\mathcal{N}(\mu, \sigma^2) \equiv$ 849 $\mathcal{N}(0, 1)\sigma + \mu$ and our definition of $\delta \varpi_{\mathrm{DR2}}$.

When the true parallax of a star is different from $\varpi_{\rm clus}$, as is the case for field stars, Δ_{ϖ} will have no dependence on $\delta \varpi_{\rm DR2}$ as $\delta \varpi_{\rm DR2} \propto \varpi_{\rm true} - \varpi_{\rm clus}$. Cluster stars, however, will show a strong correlation between Δ_{ϖ} and $\delta \varpi_{\rm DR2}$. Since $\varpi_{\rm true} = \varpi_{\rm clus}$ for cluster members, $-\delta \varpi_{\rm DR2} = -\mathcal{N}(0,1)\sigma_{\varpi_{\rm DR2}}$ and thus, $\Delta_{\varpi} \propto -\delta \varpi_{\rm DR2}$.

Figure 6 shows the distribution of $\Delta \varpi$ and $\delta \varpi_{\mathrm{DR2}}$.

Figure 6 shows the distribution of $\Delta \varpi$ and $\delta \varpi_{\mathrm{DR2}}$.

For the field stars and member stars in NGC-188 line-of
sight. We identified field stars as those with < 1% mem
bership probability; $\Delta \varpi$ has little or no dependence on $\delta \varpi_{\mathrm{DR2}}$ for these stars (filled contours). Bonafide clus
ter members (open line contours) show a strong, nega
ter members (open line contours) show a strong, nega
cluster member designation applies to those stars with

cluster membership > 50% in both our catalog and that

cluster membership > 50% in both our catalog and that

of Cantat-Gaudin et al. (2020). Using this definition,

we are confident that nothing inherent to our cluster

membership analysis is driving the correlation seen in

Figure 6.

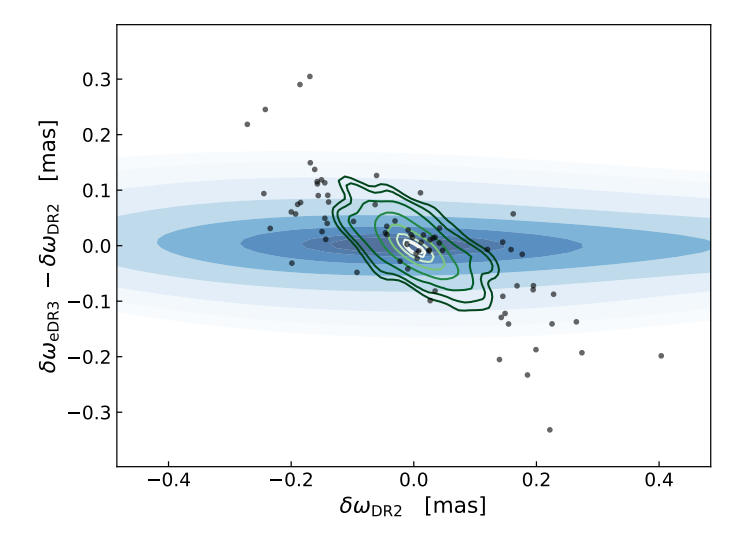


Figure 6. The observed parallax relative to the cluster in Gaia DR2 ($\delta \varpi_{\mathrm{DR2}}$) compared to the change in this relative parallax between Gaia eDR3 and DR2 for the target field containing the cluster NGC 188. Field stars (filled contours, darker colors represent higher density) show almost no correlation between these quantities. Bonafide cluster members (open contours, lighter colors denote higher density) show a strong negative correlation. Stars identified as cluster members in our analysis but absent from Cantat-Gaudin et al. (2020) are shown as individual points. See text for details.

We statistically assess the relationship shown in Figure 6 across all target fields using simple linear regression². In each target field, we fit a line to $\Delta \varpi$ vs. $\delta \omega_{\rm DR2}$ for three distinction populations – field stars, onafide cluster members, and unique cluster members. Unique cluster members are probable members (> 85\% membership probability) according to our analysis but 876 have zero cluster membership probability according to Cantat-Gaudin et al. (2020) (see the black points in Fig-878 ure 6 for an example). We attempt to match all stars onsidered in our XDGMM fits with its Gaia eDR3 coun-879 C terpart using the crossmatch provided by the Gaia team gaiaedr3.dr2_neighbourhood). To ensure a clean match, we demand that the eDR3 target is within 0.15 mas of 882 the DR2 source on the sky and that the eDR3 and DR2 Gaia magnitudes do not differ by more than 0.1 mag. 884

The resulting catalog contains $\sim 1.7 \times 10^6$ stars. Along each line of sight, we assume the true cluster parallax is the median observed parallax of the bonafide cluster members. We require at least 20 bonafide members to ensure a robust measurement of $\varpi_{\rm clus}$ and at least 15 members of any other group to perform the fitting procedure. Finally, the intercept of the linear fit must be

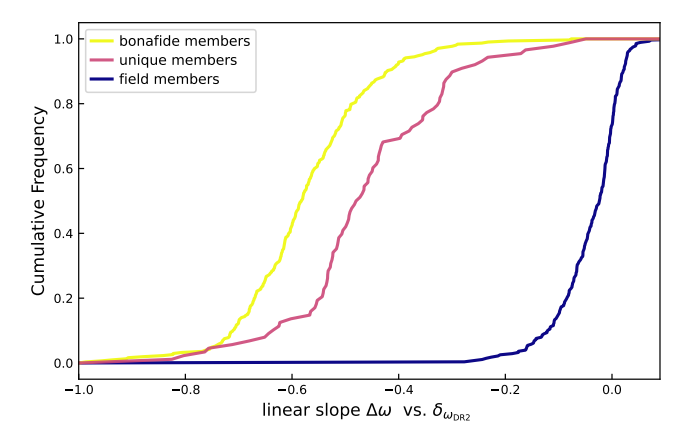


Figure 7. The distribution of linear slope fit to the $\Delta \varpi$ vs. $\delta \varpi_{\mathrm{DR2}}$ data within three stellar populations along each line of sight. The slope measures the degree of correlation between the two quantities; each line represents the empirical cumulative distribution function of slope within a population. The slope of bonafide cluster members (yellow; median of -0.58) is significantly more negative than that of field stars (blue; median of -0.02). The distribution of slope measured for cluster members uniquely identified in this work (magenta; median of -0.48) is intermediate to the field and bonafide member distributions. The similarity of the bonafide and unique cluster member slope distributions suggests that a majority of the unique cluster members are likely genuine. See text for details.

near zero to guard against significant differences in the observed parallax systematics between the two data releases (see below for details). These requirements limit our analysis to 307 sightlines for the bonafide cluster member and field populations and 88 sightlines for the unique member stars. The linear fit is performed across the same domain for all three groups. The fit only applies to stellar measurements within the extent of $\delta \varpi_{DR2}$ for cluster stars, including both bonafide and unique members. Performing the regression across the same domain ensures the most straightforward comparison between cluster and field stars.

We show the distribution of the $\Delta \varpi$ vs. $\delta \varpi_{\mathrm{DR2}}$ slope measured from the above regression for field, bonafide cluster member, and unique cluster member stars in Figver 7. The slope of the bonafide cluster members (yelver 1000 low line) is significantly negative with a median slope of -0.58. The bonafide cluster members show a strong negative correlation between the dependent and independent quantities as predicted by equation 9. However, the expected slope for a pure cluster member sample is -1. We discuss potential reasons for this deviation bever 1100. Field stars (blue line) show almost no correlation between $\Delta \varpi$ and $\delta \varpi_{\mathrm{DR2}}$; their median target field slope is -0.02. Given our assumptions, the expected slope

 $^{^2}$ as implemented by Curve_fit, a part of the SCIPY python package

971

972

 $_{917}$ value for field stars is zero and near our actual result. $_{918}$ The distribution of slopes measured for unique cluster $_{919}$ members (pink line) is much closer to that of bonafide $_{920}$ cluster members than that of field stars; the median $_{921}$ slope is -0.48.

Figure 7 presents strong evidence that the majority of 922 923 unique cluster members genuinely belong to a cluster. 924 The unique cluster members clearly show a correlation 925 between the observed parallax in Gaia eDR3 and Gaia 926 DR2 that is not seen in the field stars. The most nega-927 tive slope recorded for field stars is -0.28 for any line of 928 sight. The measured slope of the unique cluster member stars is < -0.28 in over 90% of all lines of sight consid-930 ered. Further, the similarity of the slope distributions of 931 the bonafide and unique cluster member stars suggests 932 that they are largely drawn from the same distribution 933 of cluster-relative parallax ($\delta \varpi_{DR3}$, $\delta \varpi_{DR2}$). However, 934 the distribution of slopes for the unique cluster stars is 935 not as negative as that of the bonafide cluster members. We therefore conservatively conclude between 5% and 937 45% of the unique cluster stars are possible false pos-938 itives. We identify 9,118 unique cluster member stars 939 meet the data criteria detailed within this subsection and more than 7,500 probable unique cluster member 941 stars were removed from this analysis. The increase in 942 probable cluster membership due to our unique cluster 943 stars is significant even if the false positive rate is near 944 the high-end of our estimated range.

To simplify the calculation of $\Delta \varpi$ and related quanti-946 ties, we made several assumptions that are likely incor-947 rect in detail but do not detract from our line of reason-948 ing. The Gaia reported parallax contains some system-949 atic error and is likely biased. In our calculations, we do 950 correct for the global parallax offset of 0.029mas in Gaia 951 DR2 (Lindegren et al. 2018) and 0.017mas in Gaia eDR3 952 (Lindegren et al. 2020) but then assume no additional 953 systematic errors. A significantly non-zero intercept of 954 the linear fit to $\Delta \varpi$ vs. $\delta \varpi_{\mathrm{DR2}}$ along a sightline sug-955 gest influential and dissimilar bias in the parallax mea-956 surements of the two Gaia data releases. To mitigate this where possible, we remove any sightline in which 958 the absolute value of the intercept is greater than one-959 tenth the median uncertainty in the observed parallax 960 of the population under consideration. All of the re-961 ported statistics from Figure 7 include this restriction. 962 Finally, clusters do have intrinsic width, often near the 963 scale of δ_{ϖ} for cluster members. The combination of 964 these effects contributes to the change in the slope distribution for bonafide and unique cluster members relative $_{966}$ to the expectation of -1 and likely contributes to the 967 slight negative skew seen in Figure 7 for field stars. Still, 968 the slope distributions of the bonafide member and field

969 stars are sufficiently different from that of field stars to 970 support our conclusions above.

5. PREVIOUSLY UNPUBLISHED CLUSTERS DISCOVERED WITH XDGMM

We report the serendipitous discovery of 11 previously unpublished open cluster candidates. These candidates were found as components with relatively low differential entropy within the best-fit XDGMM of the 420 target fields with a successful recovery of the central target cluster. When looking for candidates in a given field, we considered all non-target cluster components of the best-fit model that had a differential entropy within a factor of 4 of the target cluster. We find 97 components that meet this differential entropy requirement.

The low differential entropy components must pass several tests before we consider them cluster candidates. First, we check to see that the cluster is spatially compact as well compact in proper-motion.

We check compactness in proper-motion by employmotion the proper-motion dispersion check developed by
Cantat-Gaudin & Anders (2019, section 5.3). We calcumotion late the total dispersion in proper-motion for each commotion ponent and compare it to their analytical threshold. We
motion examine the on-sky spatial compactness of each candimotion date using the method of Cantat-Gaudin et al. (2018b,
motion escitor 2.3). We compare the sum of the minimum spanming tree branch lengths of the candidate cluster memmotion ber positions to those of a randomly generated position
motion distribution of the same size. We remove 44 candidates
motion that do not meet both these requirements.

We then examine the parallax and sky position distributions of the remaining 53 candidates. We calculate the slope of Δ_{ϖ} vs. $\delta_{\varpi_{\mathrm{DR2}}}$ using the probable members of each component (see Section 4.2.3 for details). Only 3 candidates do not have a slope <-0.4, which is more negative than the field members within any target field (Figure 7).

We then determine if any of the 50 candidates were previously reported using Gaia DR2 data. To do so, we checked for overlap between the Gaia DR2 source IDs of our candidate members and the source IDs of membership is ship lists from the literature. We compiled a list of all unique source IDs reported as members of any cluster by Cantat-Gaudin et al. (2018a), Cantat-Gaudin et al. (2019), Castro-Ginard et al. (2018), Castro-Ginard et al. (2019) Castro-Ginard et al. (2020), Ferreira et al. (2020), sim et al. (2019), Liu (2019), or Hunt & Reffert (2020). One or more of these studies previously identified a cluster with members from 39 of our candidates. Only 11 previously unreported candidate clusters remained.

1072

1089

1097

1105

Finally, we estimate the physical size of each candidate. We calculate a physical r50 value, the radius encompassing 50% of the candidate member stars, using
the candidate's bayesian inversion parallax distance (see
data 4.1). The 11 remaining candidates span a physical r50
value ranging from 1.15 parsecs to 11.3 parsecs, placing them in the bulk of typical open cluster sizes (see
data-Gaudin & Anders 2019, Figure 4).

The final 11 newly discovered open cluster candidates all have different parent target fields. The gaussian component associated with the candidate had either the low-logo est (6 of 11 fields) or second-lowest differential entropy to of the best-fit components.

We stress that these 11 systems are open cluster candidates. The member stars of these systems occupy a
relatively small, compact volume in the space of ϖ , $\mu_{\alpha*}$,
and μ_{δ} . All candidates passed the statistical tests mendidates below) are consistent with being open clusters. Still,
confirming these candidates as bonafide open clusters
will require dedicated observational follow-up and dedecomposite tailed investigation. The 11 clusters are called XDOCC
description of the transfer of these systems occupy a
relatively small, compact volume in the space of ϖ , $\mu_{\alpha*}$,
so the space of ω , $\mu_{\alpha*}$,

We present the color-magnitude diagrams of the 11 new open cluster candidates in Figure 8 and report their central parameters in Table 1. We get age, distance, and extinction estimates for the 11 cluster candidates by using the Auriga Neural Net developed by Kounkel et al. (2020). The Auriga neural net has been trained on Gaia DR2 photometry $[G, G_{BP}, G_{RP}]$, 2MASS (Skrut-1050 skie et al. 2006) photometry [J, H, K], and Gaia DR2 parallaxes in order to predict cluster age, distance, and interstellar extinction (A_V) . We also plot isochrones using the derived parameters from Auriga, assuming solar metallicity in Figure 8. We describe the 11 new candidates and their predicted Age, A_V , and distance from the Auriga Neural Net below.

5.0.1. XDOCC-01

1057

1064

XDOCC-01 (Figure 9, row 1) is in the target field 1059 of NGC-457. Its proper-motion overlaps with that of NGC-457. The cluster is distinct from NGC-457 within 1061 parallax-magnitude space. XDOCC-01 has an age of 1062 $\log t = 8.53 \pm 0.08$, an extinction value of A_V =0.70 \pm 1063 0.09, and a distance of 813.4 \pm 23.8pc.

5.0.2. *XDOCC-02*

XDOCC-02 (Figure 9, row 2) is located within the target field of NGC-1960. It has a clear distinct grouping within proper-motion space from NGC-1960 XDOCC-02 does overlap with NGC-1960 within parallax-magnitude space. XDOCC-02 has an age of

 $_{1070} \log t = 7.54 \pm 0.09$, an extinction value of $A_V = 0.57 \pm 0.05$, and a distance of 1330.6 ± 53.2 pc.

5.0.3. *XDOCC-03*

XDOCC-03 (Figure 9, row 3) is in the LOS of NGC-1074 2345. It is closer than NGC-2345 in parallax, with a 1075 clear separation in parallax-magnitude space. It is also a 1076 distinct group in proper-motion. XDOCC-03 has an age 1077 of $\log t = 7.28 \pm 0.09$, an extinction value of A_V =0.71 \pm 1078 0.07, and a distance of 1175.8 \pm 56.0pc.

5.0.4. XDOCC-04

XDOCC-04 (Figure 9, row 4) is located within the target field of NGC-2482. Its proper-motion grouping is separate and distinct from that of NGC-2482. The parallax-magnitude distribution is also separate from the the distribution of NGC-2482, appearing to be farther away. XDOCC-04 appears to be farther away than NGC-2482. XDOCC-04 has an age of $\log t = 7.78 \pm 0.12$, an extinction value of $A_V = 0.53 \pm 0.12$, and a distance of 2891.2 \pm 107.6pc.

5.0.5. XDOCC-05

XDOCC-05 (Figure 10, row 1) is in the target field 1091 of NGC-2533. It has a distinct separation in proper-1092 motion. It has a slight separation from NGC-2533 1093 in parallax-magnitude space, appearing to be closer. 1094 XDOCC-05 has an age of $\log t = 8.18 \pm 0.12$, an extinc-1095 tion value of A_V =0.24 \pm 0.05, and a distance of 1575.8 1096 \pm 59.7pc.

5.0.6. XDOCC-06

XDOCC-06 (Figure 10, row 2) is located within the target field of IC-2395. It has a distinct grouping in proper-motion space, as well as in parallax-magnitude space. XDOCC-06 appears to be farther away than IC-1102 2395. XDOCC-06 has an age of $\log t = 7.93 \pm 0.18$, an extinction value of A_V =1.02 \pm 0.12, and a distance of 1104 1399.1 \pm 64.0pc.

5.0.7. XDOCC-07

XDOCC-07 (Figure 10, row 3) is located within the target field of NGC-3324. It has a distinct grouping in proper-motion space, as well as in parallax-magnitude space. XDOCC-07 appears to be closer than NGC-3324. XDOCC-07 has an age of $\log t=7.86\pm0.08$, an extinction value of A_V =0.58 \pm 0.05, and a distance of 460.1 \pm 10.0pc.

5.1. XDOCC-08

XDOCC-08 (Figure 10, row 4) is located within the target field of NGC-6514. XDOCC-08 is separate

 1116 from NGC-6514 in proper-motion space. The parallax- 1117 magnitude distribution slightly overlaps with that of 1118 NGC-6514, but appears to be slightly farther away. 1119 XDOCC-08 has an age of log $t=7.52\pm~0.19,$ an extinc- 1120 tion value of ${\rm A}_V{=}2.50{\pm}~0.23,$ and a distance of 1511.9 $^{1121}~\pm~137.9{\rm pc}.$

5.1.1. XDOCC-09

1122

1130

1139

1147

Open cluster XDOCC-09 (Figure 11, row 1) is located in the Stock-1 target field. It has a distinct grouping in proper-motion, as well as in parallax-magnitude space. XDOCC-09 appears to be farther away in parallax than Stock-1. XDOCC-09 has an age of $\log t = 8.00 \pm 0.09$, an extinction value of A_V =0.66 \pm 0.08, and a distance of 552.7 \pm 15.6 pc.

5.1.2. XDOCC-10

Open cluster XDOCC-10 (Figure 11, row 2) is located in the Berkeley-87 LOS. Its distribution in parallax-magnitude space also overlaps with that of Berkeley-87. The only indication of it being a distinct cluster of stars is in proper-motion space, where there is a clear separation between the two groups. XDOCC-10 has an age of log $t=7.63\pm0.32$, an extinction value of $A_V=3.97\pm1.02$ 0.17, and a distance of 1994.9 \pm 144.7pc.

5.2. *XDOCC-11*

Open cluster XDOCC-11 (Figure 11, row 3) is located in the target field of IC-1369. It is distinct from IC-1369 in proper-motion space. Its parallax-magnitude space distribution very slightly overlaps with IC-1369, but is distinct and closer in distance. XDOCC-11 has an age of log $t=8.13\pm0.11$, an extinction value of A_V =1.37 \pm 1146 0.10, and a distance of 1761.9 \pm 89.3pc.

6. SUMMARY

In this work we present an automated application of extreme deconvolution gaussian mixture models (XDG-1150 MMs) to produce membership lists for open clusters. While extreme deconvolution has been used before in open cluster membership determination, it had not been applied within an automated pipeline to a large number 1154 (N > 400) of open clusters.

We fit a XDGMM to the Gaia $[\varpi, \mu_{\alpha*}, \mu_{\delta}]$ measurements within each target field. Extreme deconvolution measurement uncertains ties, covariances, and correlations within Gaia DR2 astrometric data and predict their intrinsic distribution. A gaussian mixture model is then fit to the underlying distribution. We successfully identify an open cluster separate from the field within the 3-dimensional astrometric space of $\mu_{\alpha*}$, μ_{δ} , and ϖ in 420 target fields out of a total initial sample of 426.

Comparison with previous literature results suggests our method is successful in identifying cluster members (Section 4.2.1). We find excellent agreement between mean cluster parameters for the 392 open clusters in our parent sample that are also reported in the catalog of Cantat-Gaudin et al. (2020). In addition, our cluster membership lists includes 98.7% of the previously reported cluster members by Cantat-Gaudin et al. (2020) for the same 392 target clusters. The combination of extreme deconvolution and gaussian mixture models also found a substantial population of new cluster members. The new members stars are fainter (an average of 1.1 magnitudes in G) than those in the literature, owing to the individual covariance matrices in model fitting.

Several types of cluster identification are noteworthy.
This work contains the first Gaia DR2-based membership lists for 11 previously known open clusters. In addition, we fit the entire astrometric volume surrounding
systems attributed to gaussian components distinct from
the target cluster, finding 50. Upon review, we find 39 of
these candidates have been previously reported as open
clusters in the literature. However, we also report the
serendipitous discovery 11 new open clusters candidates
within this work (Section 5).

This work address several properties, drawbacks, or concerns previously associated with using Gaussian Mixture Models (GMMs) to detect open clusters. The clusters ter detection performance of GMMs is sensitive to the search volume and the number of model components (Hunt & Reffert 2020). Efficiently applying GMMs or NDGMMs to a large sample of clusters requires not only non-interactive solutions to these concerns but also raises a new problem. Since the field will be represented by one or more components, any pipeline-like analysis must be able to automatically select the model component associated with the cluster.

To define the initial cluster search volume, we only require an initial central cluster position in the sky, an restimate of the projected cluster size, and any estimates of distances to extract the relevant Gaia DR2 data and perform data preprocessing. Our automated preprocessing routine conservatively defines a sufficient volume in parallax and proper-motion space, centered on the sky coordinates and distance estimates of the target cluster, designed to encapsulate all potential cluster members. This data preprocessing requires little to no fine tuning for any one cluster (Section 3.1).

We determine the number of model components and l215 cluster component using quantitative methods. We sel226 lect the best-fit XDGMM of each target field by minimiz-

ing the BIC; the best-fit model contained a component associated with the target cluster in 414/426 cases. The model component with the smallest differential entropy, a measure of compactness, was automatically selected as the target cluster. The minimal h component represented either the target cluster (385 target fields), an adjacent open cluster (22 target fields), or a new open cluster candidate (6 targets fields) in the vast majority of best-fitting models.

The differential entropy is a useful metric in finding and selecting open cluster gaussian mixture components from within a sight line. The agnostic nature of using the differential entropy over an arbitrarily chosen sigma significance will allow for greater flexibility in differentiating the astrometric over-density that constitute most open clusters in the Milky Way.

In this work we have shown how XDGMM can be an effective and capable method to calculate compresions hensive membership probabilities across a multitude of open cluster morphologies. Moving forward, we plan to use what we learned from automating fitting with XDGMM to calculate membership lists for a larger sample of known open clusters in the Milky Way in order to fully take advantage of the greater completeness and exquisite data quality that Gaia eDR3 offers.

7. ACKNOWLEDGEMENTS

The authors thank the referee for the comments and suggestions, which have greatly improved the quality of this paper. KOJ thanks the LSSTC Data Science Fellowship Program, which is funded by LSSTC, NSF Cybertraining Grant #1829740, the Brinson Foundation, late and the Moore Foundation; their participation in the program has benefited this work. JB was supported in part by Vanderbilt University through the Stevenson Postdoctoral Fellowship. KHB was supported by NSF late Grant AST-1358862.

This work has made use of data from the Euro1254 pean Space Agency (ESA) mission *Gaia* (https://www.
1255 cosmos.esa.int/gaia), processed by the *Gaia* Data Pro1256 cessing and Analysis Consortium (DPAC, https://www.
1257 cosmos.esa.int/web/gaia/dpac/consortium). Funding
1258 for the DPAC has been provided by national institu1259 tions, in particular the institutions participating in the
1260 *Gaia* Multilateral Agreement.

This research made use of Astropy, a communitydeveloped core Python package for Astronomy (PriceWhelan et al. 2018; Robitaille et al. 2013), Astroquery
(Ginsburg et al. 2019), the IPython package (Perez &
Granger 2007), matplotlib, a Python library for publication quality graphics (Hunter 2007), NumPy (Harlef ris et al. 2020), pandas (McKinney 2011, 2010), Sciklication (Pedregosa et al. 2015), and SciPy (Virtanen
lef et al. 2020).

REFERENCES

1306

1242

```
1270 Ahmed, N. A., & Gokhale, D. V. 1989, IEEE Transactions
      on Information Theory, 35, 688, doi: 10.1109/18.30996
1272 Ahumada, J. A., & Lapasset, E. 2007, Astronomy and
      Astrophysics, 463, 789, doi: 10.1051/0004-6361:20054590
1273
    Allison, R. J., Goodwin, S. P., Parker, R. J., et al. 2009,
1274
      Monthly Notices of the Royal Astronomical Society, 395,
1275
      1449, doi: 10.1111/j.1365-2966.2009.14508.x
1276
   Angelo, M. S., Santos, J. F. C., Corradi, W. J. B., & Maia,
1277
      F. F. S. 2019, Astronomy & Astrophysics, 624, A8,
1278
      doi: 10.1051/0004-6361/201832702
1279
1280 Babusiaux, C., Van Leeuwen, F., Barstow, M. A., et al.
      2018, Astronomy and Astrophysics, 616, 1,
1281
      doi: 10.1051/0004-6361/201832843
1282
1283 Bailer-Jones, C. A. L. 2015, Publications of the
      Astronomical Society of the Pacific, 127, 994,
1284
      doi: 10.1086/683116
1285
1286 Bossini, D., Vallenari, A., Bragaglia, A., et al. 2019,
      Astronomy & Astrophysics, 623, A108,
1287
      doi: 10.1051/0004-6361/201834693
1288
```

```
1289 Bovy, J., Hogg, D. W., & Roweis, S. T. 2011, Annals of
      Applied Statistics, 5, 1657, doi: 10.1214/10-AOAS439
1291 Brown, A. G., Vallenari, A., Prusti, T., & de Bruijne, J. H.
     2020, Astronomy & Astrophysics, 649, A1,
1292
     doi: 10.1051/0004-6361/202039657
1294 Brown, A. G. A., Vallenari, A., Prusti, T., et al. 2018,
      Astronomy & Astrophysics, 616, A1,
1295
     doi: 10.1051/0004-6361/201833051
1296
   Cabrera-Cano, J., & Alfaro, E. J. 1990, Astronomy and
1297
     Astrophysics, 235, 94
1299 Cantat-Gaudin, T., & Anders, F. 2019, 1.
     http://arxiv.org/abs/1911.07075
   Cantat-Gaudin, T., Jordi, C., Vallenari, A., et al. 2018a,
1301
     Astronomy & Astrophysics, 618, A93,
1302
     doi: 10.1051/0004-6361/201833476
   Cantat-Gaudin, T., Vallenari, A., Sordo, R., et al. 2018b,
1304
1305
     Astronomy & Astrophysics, 615, A49,
```

doi: 10.1051/0004-6361/201731251

```
Cantat-Gaudin, T., Krone-Martins, A., Sedaghat, N., et al.
1307
      2019, Astronomy and Astrophysics, 624,
1308
      doi: 10.1051/0004-6361/201834453
1309
1310 Cantat-Gaudin, T., Anders, F., Castro-Ginard, A., et al.
      2020. http://arxiv.org/abs/2004.07274
1311
1312 Castro-Ginard, A., Jordi, C., Luri, X., Cantat-Gaudin, T.,
      & Balaguer-Núñez, L. 2019, 1.
1313
      http://arxiv.org/abs/1905.06161
1314
   Castro-Ginard, A., Jordi, C., Luri, X., et al. 2018, 1,
1315
      doi: 10.1051/0004-6361/201833390
1316
     -. 2020, Astronomy and Astrophysics, 635, 1,
1317
      doi: 10.1051/0004-6361/201937386
1318
    Oaszykowski, M., & Walczak, B. 2009, in Comprehensive
1319
      Chemometrics, Vol. 2, 635-654,
1320
      doi: 10.1016/B978-044452701-1.00067-3
1321
1322 Dias, W. S., Monteiro, H., & Assafin, M. 2018, Monthly
      Notices of the Royal Astronomical Society, 478, 5184,
1323
      doi: 10.1093/mnras/sty1456
1324
1325 Dias, W. S., Monteiro, H., Caetano, T. C., et al. 2014,
      Astronomy & Astrophysics, 564, A79,
1326
      doi: 10.1051/0004-6361/201323226
1327
1328 Feigelson, E. D., Getman, K. V., Townsley, L. K., et al.
      2011, Astrophysical Journal, Supplement Series, 194,
1329
      doi: 10.1088/0067-0049/194/1/9
1330
1331 Ferreira, F. A., Corradi, W. J. B., Maia, F. F. S., Angelo,
      M. S., & Santos, J. F. C. 2020, Monthly Notices of the
1332
      Royal Astronomical Society, 496, 2021,
1333
      doi: 10.1093/mnras/staa1684
1334
    Friel, E. 1995, Annual Review of Astronomy and
1335
      Astrophysics, 33, 381,
1336
1337
      doi: 10.1146/annurev.astro.33.1.381
    Gao, X. 2018, The Astronomical Journal, 156, 121,
1338
      doi: 10.3847/1538-3881/aad690
1339
1340 Ghosh, Jayanta K., Delampady, M., & Samanta, T. 2006
      (Springer), doi: 10.1198/jasa.2008.s232
1341
   Ginsburg, A., Sipőcz, B. M., Brasseur, C. E., et al. 2019,
1342
      arXiv, 98, 1, doi: 10.3847/1538-3881/aafc33
1343
1344 Girardi, L., Bressan, A., Bertelli, G., & Chiosi, C. 2000,
      Astronomy and Astrophysics Supplement Series, 141,
1345
      371, doi: 10.1051/aas:2000126
1346
1347 Hao, J., Koester, B. P., McKay, T. A., et al. 2009,
      Astrophysical Journal, 702, 745,
1348
      doi: 10.1088/0004-637X/702/1/745
1349
1350 Harris, C. R., Millman, K. J., Walt, S. J. V. D., et al. 2020,
      Nature, 585, 357, doi: 10.1038/s41586-020-2649-2
1351
1352 He, M. Y., & Petrovich, C. 2017, 12, 1,
      doi: 10.1093/mnras/stx2718
1353
1354 Hillenbrand, L. A., & Hartmann, L. W. 1998, The
      Astrophysical Journal, 492, 540, doi: 10.1086/305076
```

```
1356 Holoien, T. W. S., Marshall, P. J., & Wechsler, R. H. 2016,
     eprint arXiv:1611.00363, 153, 249,
1357
     doi: 10.3847/1538-3881/aa68a1
1358
   Huber, P. J. 1980, Robust statistics / Peter J. Huber.,
1359
      Wiley series in probability and mathematical statistics
1360
      (New York: Wiley)
1361
1362 Hunt, E. L., & Reffert, S. 2020,
     doi: 10.1051/0004-6361/202039341
   Hunter, J. D. 2007, Computing in Science and Engineering,
     9, 90, doi: 10.1109/MCSE.2007.55
   Johnson, H. L., & Knuckles, C. F. 1955, The Astrophysical
     Journal, 122, 209
   Kharchenko, N. V., Piskunov, A. E., Schilbach, E., Röser,
     S., & Scholz, R. D. 2013, Astronomy and Astrophysics,
     558, 1, doi: 10.1051/0004-6361/201322302
1370
1371 Kos, J., de Silva, G., Buder, S., et al. 2018, Monthly
     Notices of the Royal Astronomical Society, 480, 5242,
1372
     doi: 10.1093/MNRAS/STY2171
1373
   Kounkel, M., Covey, K., & Stassun, K. G. 2020, arXiv,
1374
     doi: 10.3847/1538-3881/abc0e6
1375
1376 Kroupa, P. 2001, From Darkness to Light: Origin and
     Evolution of Young Stellar Clusters, 243, 1.
1377
     https://arxiv.org/abs/0010405v2
1378
1379 Kuhn, M. A., Medina, N., Getman, K. V., et al. 2017
1380 Kuhn, M. A., Feigelson, E. D., Getman, K. V., et al. 2014,
      Astrophysical Journal, 787,
1381
     doi: 10.1088/0004-637X/787/2/107
1382
   Lindegren, L. 2019, arXiv,
1383
     doi: 10.1051/0004-6361/201936161
   Lindegren, L., Hernández, J., Bombrun, A., et al. 2018,
     Astronomy and Astrophysics, 616, 1,
     doi: 10.1051/0004-6361/201832727
   Lindegren, L., Bastian, U., Biermann, M., et al. 2020, Gaia
     Early Data Release 3: Parallax bias versus magnitude,
     colour, and position. http://arxiv.org/abs/2012.01742
1390
1391 Liu, C. 2019, 17, 1
1392 Liu, L., & Pang, X. 2019. http://arxiv.org/abs/1910.12600
1393 Luri, X., Brown, A. G., Sarro, L. M., et al. 2018,
     Astronomy and Astrophysics, 616, 1,
1394
     doi: 10.1051/0004-6361/201832964
1395
1396 McKinney, W. 2010, Proceedings of the 9th Python in
     Science Conference, 1, 56,
1397
     doi: 10.25080/majora-92bf1922-00a
1398
     -. 2011, Python for High Performance and Scientific
1399
     Computing, 1
1400
   Olivares, J., Bouy, H., Sarro, L. M., et al. 2019, Astronomy
1401
     and Astrophysics, 625, A115,
1402
     doi: 10.1051/0004-6361/201834924
1403
   Pang, X., Li, Y., Yu, Z., et al. 2021,
```

doi: 10.3847/1538-4357/abeaac

1405

```
1406 Pearson, K. 1893, Bulletin of Mathematical Biology, 185,
      doi: https://doi.org/10.1098/rsta.1894.0003
1407
1408 Pedregosa, F., Varoquaux, G., Buitinck, L., et al. 2015,
      GetMobile: Mobile Computing and Communications, 19,
1409
      29, doi: 10.1145/2786984.2786995
1410
    Perets, H. B. 2015, 251–275,
1411
      doi: 10.1007/978-3-662-44434-4{_}11
1412
1413 Perez, F., & Granger, B. E. 2007, Computing in Science &
      Engineering, 9, 21, doi: 10.1109/MCSE.2007.53
1414
    Price-Whelan, A. M., Nidever, D. L., Choi, Y., et al. 2019,
1415
      The Astrophysical Journal, 887, 19,
1416
      doi: 10.3847/1538-4357/ab4bdd
1417
     Price-Whelan, A. M., Sipőcz, B. M., Günther, H. M., et al.
1418 I
      2018, The Astronomical Journal, 156, 123,
1419
      doi: 10.3847/1538-3881/aabc4f
1420
    Prusti, T., de Bruijne, J. H. J., Brown, A. G. A., et al.
1421
      2016, Astronomy & Astrophysics, 595, A1,
1422
      doi: 10.1051/0004-6361/201629272
1423
1424 Riello, M., De Angeli, F., Evans, D. W., et al. 2018,
      Astronomy and Astrophysics, 616, 1,
1425
      doi: 10.1051/0004-6361/201832712
1426
1427 Robitaille, T. P., Tollerud, E. J., Greenfield, P., et al. 2013,
      Astronomy & Astrophysics, 558, A33,
1428
      doi: 10.1051/0004-6361/201322068
1429
```

```
1430 Sim, G., Lee, S. H., Ann, H. B., & Kim, S. 2019, Journal of
     the Korean Astronomical Society, 52, 145,
     doi: 10.5303/JKAS.2019.52.5.145
1433 Skrutskie, M. F., Cutri, R. M., Stiening, R., et al. 2006, The
     Astronomical Journal, 131, 1163, doi: 10.1086/498708
1435 Spina, L., Ting, Y.-S., De Silva, G. M., et al. 2021, Monthly
     Notices of the Royal Astronomical Society, 503, 3279,
     doi: 10.1093/mnras/stab471
1437
1438 Toonen, S., Portegies Zwart, S., Hamers, A. S., &
     Bandopadhyay, D. 2020, arXiv, 16
1439
   Utsunomiya, M., Hashimoto, M., & Kajitani, H. 1996, NEC
1440
     Research and Development, 37, 369
   Vasiliev, E. 2019, Monthly Notices of the Royal
1442
     Astronomical Society, 489, 623,
1443
     doi: 10.1093/mnras/stz2100
1444
   Virtanen, P., Gommers, R., Oliphant, T. E., et al. 2020,
```

Nature Methods, 17, 261, doi: 10.1038/s41592-019-0686-2

Wenger, M., Ochsenbein, F., Egret, D., et al. 2000, 22, 9,

doi: 10.1051/aas:2000332

Table 1. Cluster parameters for 11 open clusters confirmed in this work and 11 newly discovered open clusters. All σ values in this table are median absolute deviations (MAD) multiplied by the factor 1.4826 to approximate a standard deviation. The 'dmode₁₆' and 'dmode₈₄' values are the 16th and 84th percentiles of the distance posterior distribution. 'dmode' is the 50th percentile of the distance posterior distribution. The full table of 431 cluster parameters will be made available electronically.

Name	α	δ	$\overline{\omega}$	σ_{arpi}	$\mu_{\alpha*}$	$\sigma_{\mu_{lpha*}}$	μ_{δ}	σ_{μ_δ}	$N_{p>0.85}$	r_{50}	$dmode_{16}$	dmode	dmode ₈₄	R_{GC}	Z_{GC}
	\deg	\deg	mas	mas	mas/yr	mas/yr	mas/yr	mas/yr		\deg	kpc	kpc	kpc	kpc	kpc
Berkeley-42	286.31	1.90	0.09	0.11	-2.84	0.26	-5.95	0.25	236	0.02	10.460	11.041	11.621	6.54	-0.43
Bochum-1	96.33	19.90	0.23	0.06	-0.19	0.08	-0.43	0.07	29	0.13	4.477	4.586	4.695	12.81	0.32
Bochum-14	270.52	-23.70	0.31	0.09	0.25	0.13	-1.06	0.10	107	0.13	3.050	3.083	3.116	5.25	-0.01
Bochum-7	131.10	-45.97	0.18	0.03	-3.09	0.10	3.65	0.15	59	0.19	5.405	5.484	5.563	10.32	-0.16
Collinder-96	97.62	2.84	0.12	0.07	0.13	0.29	0.38	0.36	57	0.11	7.895	8.257	8.619	16.05	-0.43
NGC-1931	82.80	34.24	0.45	0.05	0.37	0.12	-1.91	0.19	27	0.09	2.227	2.262	2.298	10.55	0.04
NGC-2467	118.18	-26.37	0.19	0.03	-2.55	0.08	2.58	0.11	154	0.09	5.093	5.169	5.245	11.59	0.08
NGC-3247	156.71	-57.93	0.32	0.11	-6.49	1.20	3.02	0.60	225	0.05	2.967	2.986	3.006	8.08	0.01
NGC-6514	270.65	-22.90	0.85	0.04	0.33	0.32	-1.68	0.20	113	0.23	1.169	1.174	1.179	7.14	0.02
Trumpler-24	254.01	-40.47	0.84	0.02	0.49	0.62	-1.80	0.54	19	0.49	1.194	1.202	1.209	7.15	0.06
Trumpler-27	264.08	-33.49	0.49	0.01	-0.15	0.08	-1.28	0.06	20	0.20	2.003	2.032	2.061	6.28	-0.01
XDOCC-01	19.90	58.35	1.26	0.06	-1.68	0.11	-0.34	0.06	22	0.17	0.788	0.796	0.805	8.80	-0.03
XDOCC-02	84.05	34.30	0.80	0.05	0.28	0.11	-2.29	0.07	26	0.14	1.215	1.261	1.311	9.57	0.06
XDOCC-03	107.01	-13.05	0.88	0.04	-3.32	0.36	0.55	0.13	25	0.21	1.121	1.140	1.159	8.95	-0.02
XDOCC-04	118.83	-24.17	0.33	0.04	-2.71	0.08	3.06	0.09	60	0.21	2.848	3.023	3.221	10.06	0.14
XDOCC-05	121.75	-29.90	0.60	0.02	-3.66	0.05	3.56	0.03	19	0.12	1.590	1.636	1.685	9.06	0.07
XDOCC-06	130.93	-48.15	0.77	0.04	-6.38	0.11	3.61	0.09	33	0.06	1.271	1.299	1.327	8.47	-0.05
XDOCC-07	159.48	-58.72	2.28	0.04	-14.32	0.23	0.93	0.23	21	0.15	0.433	0.436	0.439	8.01	0.02
XDOCC-08	270.76	-22.73	0.73	0.05	0.67	0.11	-2.57	0.08	51	0.12	1.320	1.348	1.377	6.79	0.01
XDOCC-09	293.60	25.00	1.83	0.04	-0.46	0.10	-8.74	0.37	47	0.66	0.546	0.550	0.553	8.04	0.05
XDOCC-10	305.42	37.29	0.51	0.06	-2.39	0.11	-5.23	0.12	40	0.16	1.884	1.919	1.956	7.87	0.03
XDOCC-11	317.73	47.72	0.47	0.04	-1.01	0.05	-1.74	0.05	21	0.10	1.999	2.063	2.131	8.54	0.02

1449 APPENDIX

A. COLOR MAGNITUDE DIAGRAMS OF 11 NEWLY DISCOVERED OPEN CLUSTER
B. FOUR PLOTS OF 11 NEWLY DISCOVERED OPEN CLUSTERS

REFERENCES

Ahmed, N. A., & Gokhale, D. V. 1989, IEEE Transactions
on Information Theory, 35, 688, doi: 10.1109/18.30996
Ahumada, J. A., & Lapasset, E. 2007, Astronomy and
Astrophysics, 463, 789, doi: 10.1051/0004-6361:20054590
Allison, R. J., Goodwin, S. P., Parker, R. J., et al. 2009,
Monthly Notices of the Royal Astronomical Society, 395,
1458
1449, doi: 10.1111/j.1365-2966.2009.14508.x

1450

1451

- 1459 Angelo, M. S., Santos, J. F. C., Corradi, W. J. B., & Maia,
- 1460 F. F. S. 2019, Astronomy & Astrophysics, 624, A8,
- doi: 10.1051/0004-6361/201832702
- 1462 Babusiaux, C., Van Leeuwen, F., Barstow, M. A., et al.
- ¹⁴⁶³ 2018, Astronomy and Astrophysics, 616, 1,
- doi: 10.1051/0004-6361/201832843

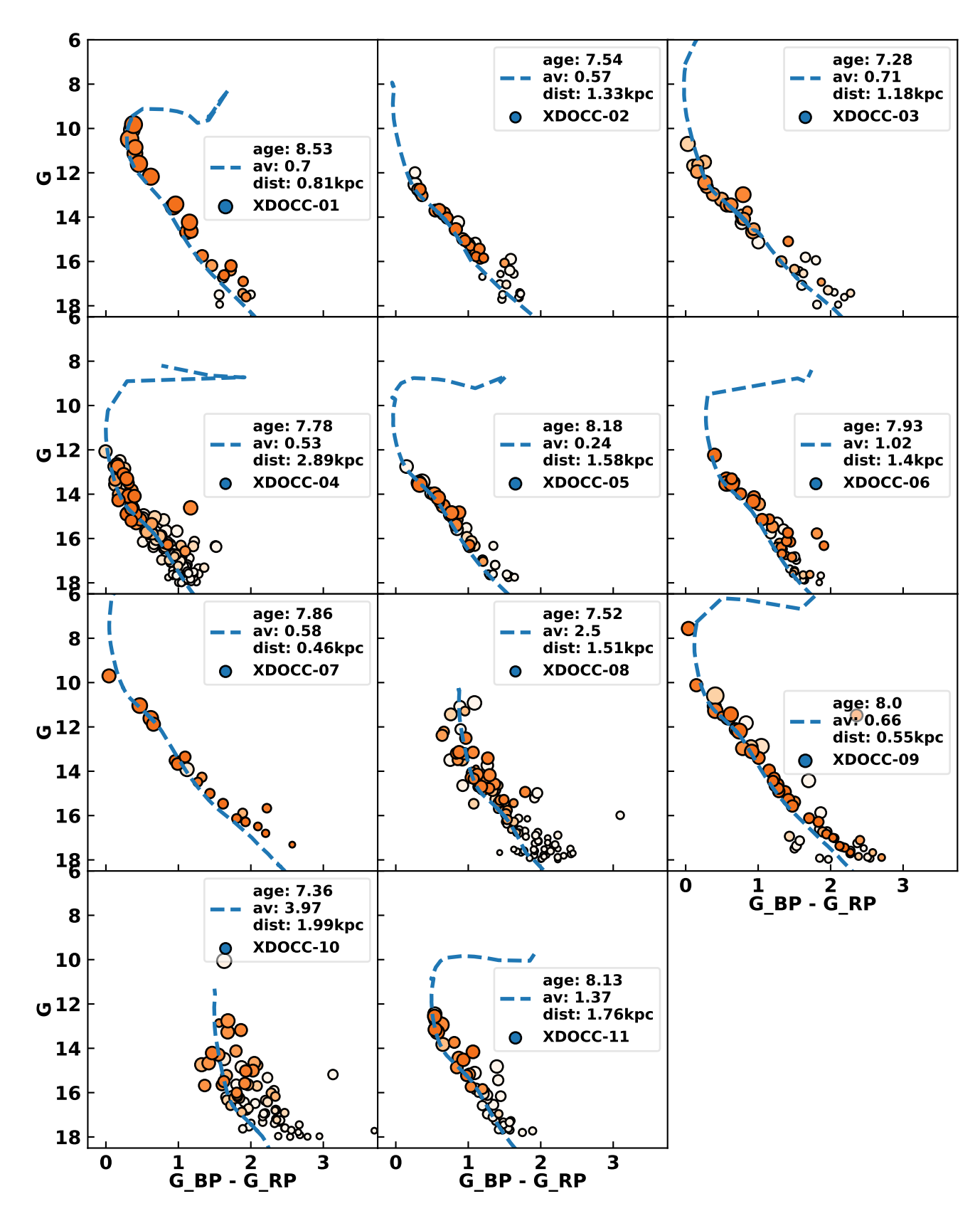


Figure 8. Multi plot color-magnitude diagrams of the 11 newly discovered open clusters within this work. Cluster member stars are plotted as orange colored points. The points are colored by their membership probability, where darker colors == higher probability. The points are sized by their G_{BP} - G_{RP} uncertainty, where bigger == lower uncertainty. The isochrone age, distance, and extinction values are predictions from the Auriga Neural Net developed by Kounkel et al. (2020). All isochrones have been set to a solar metallicity.

Table 2. Individual membership measurements for 10 member stars within 10 clusters within this catalog. All columns except for Cluster and P_{mem} are directly downloaded from the Gaia DR2 archive. The full member star catalog will be made available electronically.

Cluster	ID_{GDR2}	α	δ	ϖ	σ_{arpi}	$\mu_{\alpha*}$	$\sigma_{\mu_{lpha*}}$	μ_{δ}	σ_{μ_δ}	G	$G_{BP}-G_{RP}$	P_{mem}
		\deg	\deg	mas	mas	mas/yr	mas/yr	mas/yr	mas/yr	mag	mag	
Berkeley_104	431611438369749376	0.817	63.580	0.212	0.025	-2.397	0.042	0.022	0.039	14.810	1.648	1.00
Berkeley_66	461225237865057792	46.072	58.710	0.163	0.072	-0.802	0.154	0.153	0.127	16.808	1.717	0.91
$Berkeley_70$	194973343236220544	81.454	41.925	0.015	0.123	0.939	0.224	-1.927	0.160	17.469	1.362	0.90
Collinder_ 394	4085955053336931840	283.095	-19.961	1.205	0.189	-1.067	0.332	-5.679	0.273	17.821	1.780	0.74
$IC_{-}166$	511352282214681216	27.643	61.804	0.167	0.088	-1.611	0.092	1.303	0.116	17.294	1.569	0.98
NGC_188	573748841233408384	14.078	85.085	0.528	0.075	-2.601	0.176	-0.775	0.110	17.243	1.242	0.97
NGC_2099	3451182079777549568	88.032	32.572	0.547	0.037	2.108	0.079	-5.848	0.066	10.673	0.243	0.76
NGC_2158	3426177016401394944	91.734	24.098	0.113	0.164	-0.283	0.255	-2.350	0.218	17.830	1.290	0.74
NGC_2439	5598104289661179648	115.143	-31.693	0.254	0.118	-2.240	0.176	3.170	0.197	17.724	1.149	0.88
NGC_2539	5726703685031241344	122.592	-13.175	0.764	0.032	-2.378	0.047	-0.593	0.032	15.039	0.804	1.00

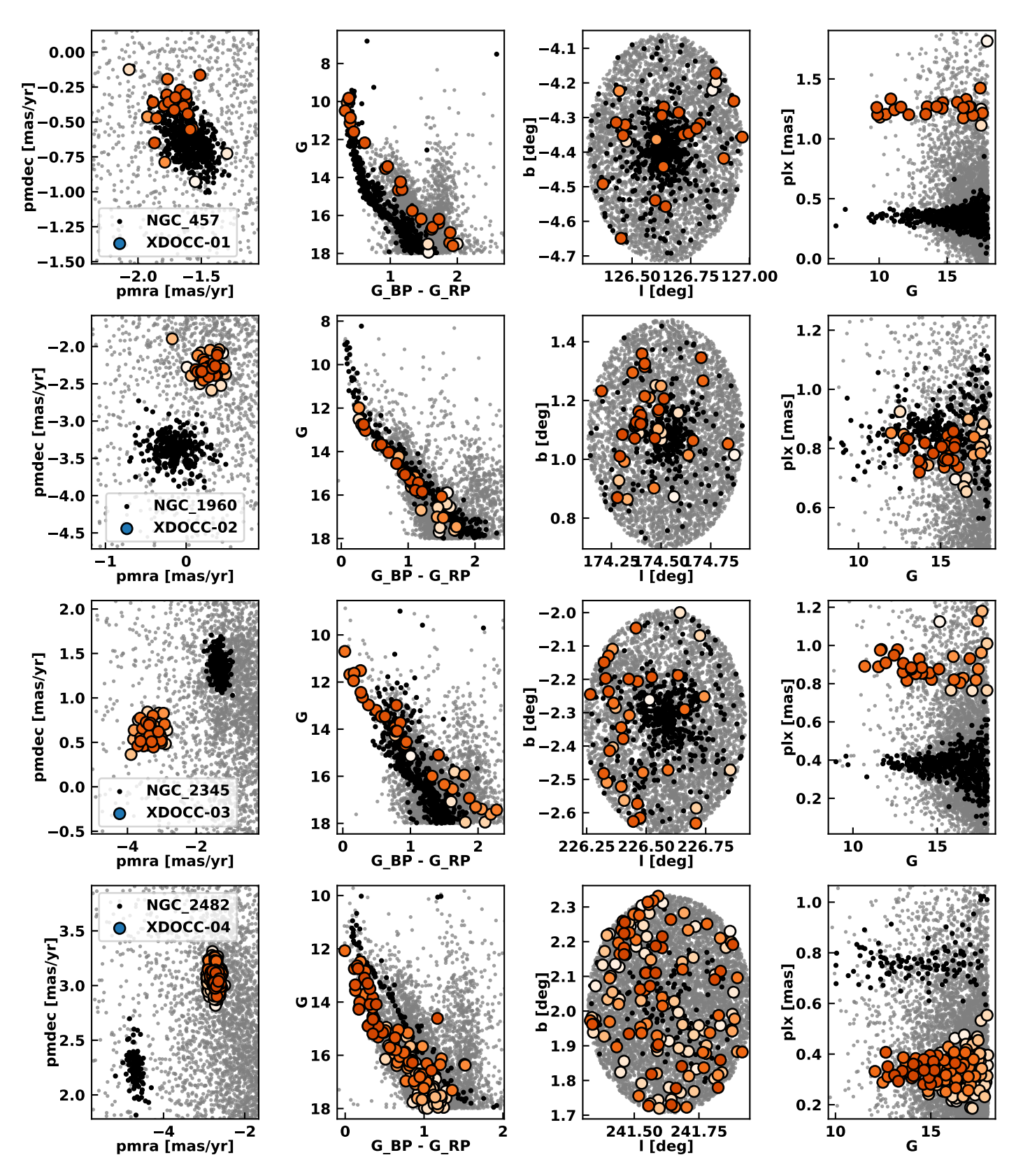


Figure 9. Four plots for newly discovered XDOCC clusters [1-4]. Each cluster candidate gets a row in the figure. The first column of plots are proper motion vector plots. The second column are all Gaia DR2 G_{BP} - G_{RP} color and G-band magnitude plots. The third columns are the cluster galactic positions (l, b) in the sky. The fourth column are all parallax-magnitude plots. The XDOCC cluster is plotted as orange colored circles in all plots with the darker colors == higher membership probability. The targeted cluster found within the target field is plotted as black dots. The field is plotted in the background as small gray dots.

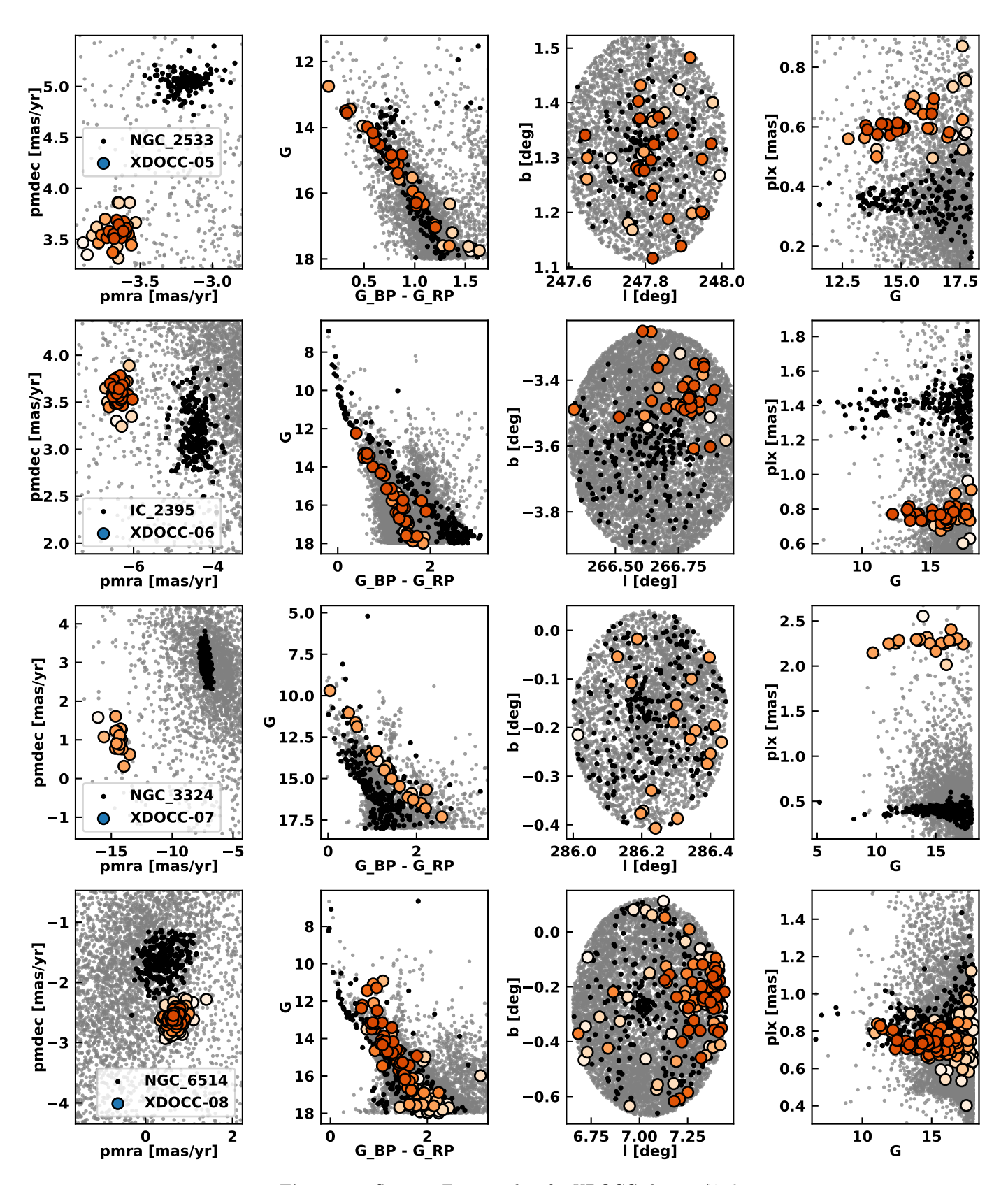


Figure 10. Same as Figure 9, but for XDOCC clusters [4-8].

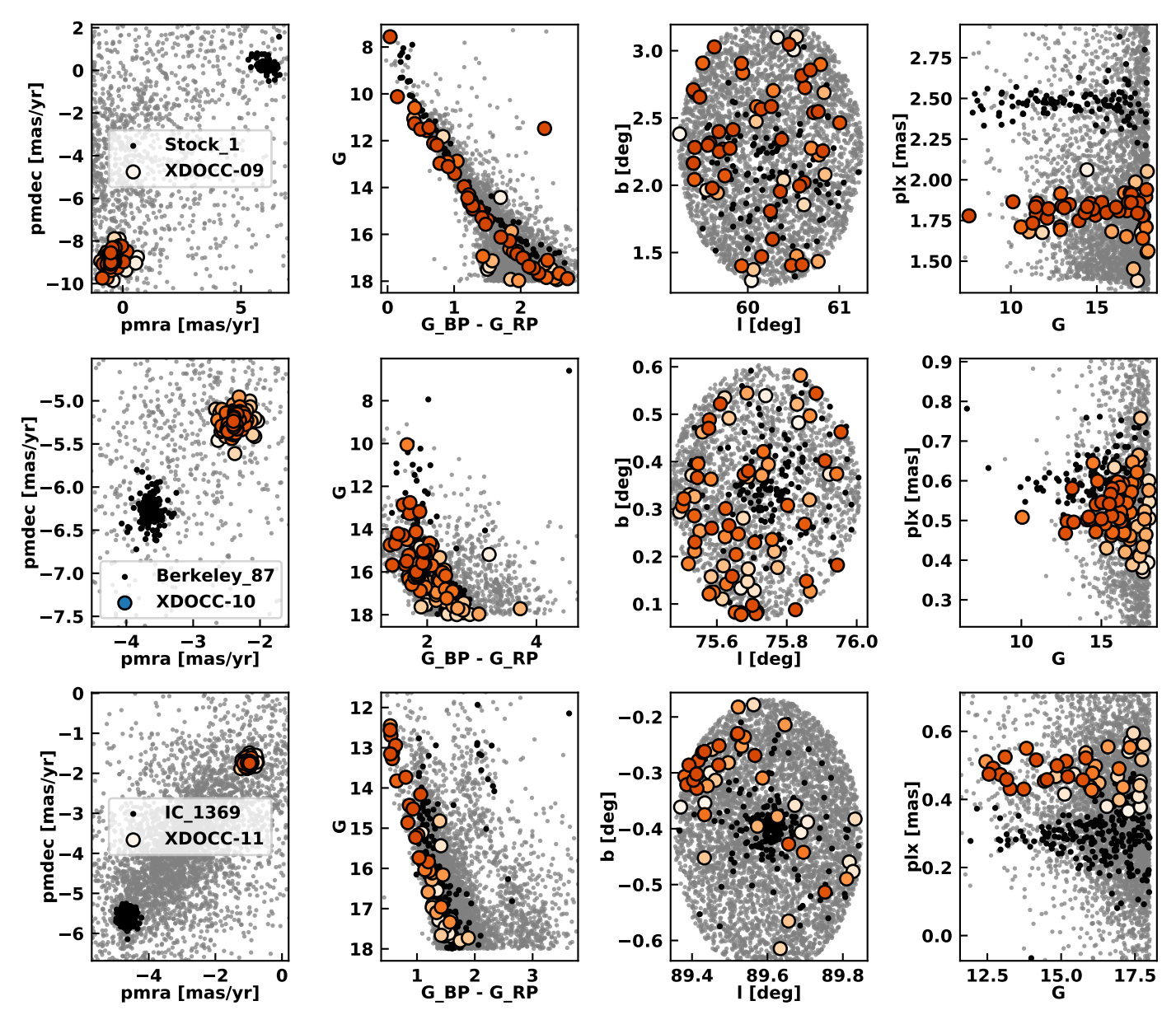


Figure 11. Same as Figure 10, but for XDOCC clusters [9-11].

1465 Bailer-Jones, C. A. L. 2015, Publications of the 1476 Brown, A. G. A., Vallenari, A., Prusti, T., et al. 2018, Astronomical Society of the Pacific, 127, 994, 1477 Astronomy & Astrophysics, 616, A1, 1466 doi: 10.1051/0004-6361/201833051 1478 doi: 10.1086/683116 1467 Cabrera-Cano, J., & Alfaro, E. J. 1990, Astronomy and 1479 1468 Bossini, D., Vallenari, A., Bragaglia, A., et al. 2019, Astrophysics, 235, 94 1480 Astronomy & Astrophysics, 623, A108, 1469 Cantat-Gaudin, T., & Anders, F. 2019, 1. 1481 doi: 10.1051/0004-6361/201834693 1470 $\rm http://arxiv.org/abs/1911.07075$ 1482 Cantat-Gaudin, T., Jordi, C., Vallenari, A., et al. 2018a, 1471 Bovy, J., Hogg, D. W., & Roweis, S. T. 2011, Annals of 1483 Astronomy & Astrophysics, 618, A93, 1484 Applied Statistics, 5, 1657, doi: 10.1214/10-AOAS439 1472 $\mathbf{doi:}\ 10.1051/0004\text{-}6361/201833476$ 1485 1473 Brown, A. G., Vallenari, A., Prusti, T., & de Bruijne, J. H. Cantat-Gaudin, T., Vallenari, A., Sordo, R., et al. 2018b, 2020, Astronomy & Astrophysics, 649, A1, 1474 Astronomy & Astrophysics, 615, A49, 1487

1475

```
Cantat-Gaudin, T., Krone-Martins, A., Sedaghat, N., et al.
1489
      2019. Astronomy and Astrophysics, 624.
1490
                                                                      1539
      doi: 10.1051/0004-6361/201834453
                                                                      1540
1491
1492 Cantat-Gaudin, T., Anders, F., Castro-Ginard, A., et al.
                                                                      1541
      2020. http://arxiv.org/abs/2004.07274
                                                                      1542
1493
                                                                            (New York: Wiley)
   Castro-Ginard, A., Jordi, C., Luri, X., Cantat-Gaudin, T.,
                                                                      1543
      & Balaguer-Núñez, L. 2019, 1.
                                                                      1544
1495
      http://arxiv.org/abs/1905.06161
1496
   Castro-Ginard, A., Jordi, C., Luri, X., et al. 2018, 1,
      doi: 10.1051/0004-6361/201833390
     -. 2020, Astronomy and Astrophysics, 635, 1,
1499
                                                                            Journal, 122, 209
                                                                      1549
      doi: 10.1051/0004-6361/201937386
1500
                                                                      1550
     Oaszykowski, M., & Walczak, B. 2009, in Comprehensive
1501
      Chemometrics, Vol. 2, 635-654,
1502
                                                                      1552
      doi: 10.1016/B978-044452701-1.00067-3
1503
1504 Dias, W. S., Monteiro, H., & Assafin, M. 2018, Monthly
                                                                      1554
      Notices of the Royal Astronomical Society, 478, 5184,
1505
                                                                      1555
      doi: 10.1093/mnras/sty1456
1506
                                                                      1556
1507 Dias, W. S., Monteiro, H., Caetano, T. C., et al. 2014,
                                                                      1557
      Astronomy & Astrophysics, 564, A79,
1508
      doi: 10.1051/0004-6361/201323226
1509
                                                                      1559
1510 Feigelson, E. D., Getman, K. V., Townsley, L. K., et al.
                                                                      1560
      2011, Astrophysical Journal, Supplement Series, 194,
1511
      doi: 10.1088/0067-0049/194/1/9
1512
1513 Ferreira, F. A., Corradi, W. J. B., Maia, F. F. S., Angelo,
                                                                      1563
      M. S., & Santos, J. F. C. 2020, Monthly Notices of the
1514
                                                                      1564
      Royal Astronomical Society, 496, 2021,
1515
                                                                      1565
      doi: 10.1093/mnras/staa1684
1516
1517 Friel, E. 1995, Annual Review of Astronomy and
                                                                      1567
      Astrophysics, 33, 381,
1518
      doi: 10.1146/annurev.astro.33.1.381
1519
   Gao, X. 2018, The Astronomical Journal, 156, 121,
1520
                                                                      1570
      doi: 10.3847/1538-3881/aad690
1521
                                                                      1571
1522 Ghosh, Jayanta K., Delampady, M., & Samanta, T. 2006
                                                                      1572
      (Springer), doi: 10.1198/jasa.2008.s232
1523
                                                                      1573 Liu, C. 2019, 17, 1
   Ginsburg, A., Sipőcz, B. M., Brasseur, C. E., et al. 2019,
1524
      arXiv, 98, 1, doi: 10.3847/1538-3881/aafc33
1525
1526 Girardi, L., Bressan, A., Bertelli, G., & Chiosi, C. 2000,
                                                                      1576
      Astronomy and Astrophysics Supplement Series, 141,
1527
                                                                      1577
      371, doi: 10.1051/aas:2000126
1528
1529 Hao, J., Koester, B. P., McKay, T. A., et al. 2009,
                                                                      1579
      Astrophysical Journal, 702, 745,
1530
                                                                      1580
      doi: 10.1088/0004-637X/702/1/745
1531
                                                                      1581
1532 Harris, C. R., Millman, K. J., Walt, S. J. V. D., et al. 2020,
                                                                            Computing, 1
                                                                      1582
      Nature, 585, 357, doi: 10.1038/s41586-020-2649-2
1533
                                                                      1583
1534 He, M. Y., & Petrovich, C. 2017, 12, 1,
                                                                      1584
      doi: 10.1093/mnras/stx2718
1535
                                                                      1585
1536 Hillenbrand, L. A., & Hartmann, L. W. 1998, The
      Astrophysical Journal, 492, 540, doi: 10.1086/305076
                                                                            doi: 10.3847/1538-4357/abeaac
                                                                      1587
1537
```

```
1538 Holoien, T. W. S., Marshall, P. J., & Wechsler, R. H. 2016,
     eprint arXiv:1611.00363, 153, 249,
     doi: 10.3847/1538-3881/aa68a1
   Huber, P. J. 1980, Robust statistics / Peter J. Huber.,
     Wiley series in probability and mathematical statistics
   Hunt, E. L., & Reffert, S. 2020,
     doi: 10.1051/0004-6361/202039341
   Hunter, J. D. 2007, Computing in Science and Engineering,
     9, 90, doi: 10.1109/MCSE.2007.55
   Johnson, H. L., & Knuckles, C. F. 1955, The Astrophysical
   Kharchenko, N. V., Piskunov, A. E., Schilbach, E., Röser,
     S., & Scholz, R. D. 2013, Astronomy and Astrophysics,
     558, 1, doi: 10.1051/0004-6361/201322302
1553 Kos, J., de Silva, G., Buder, S., et al. 2018, Monthly
     Notices of the Royal Astronomical Society, 480, 5242,
     doi: 10.1093/MNRAS/STY2171
   Kounkel, M., Covey, K., & Stassun, K. G. 2020, arXiv,
     doi: 10.3847/1538-3881/abc0e6
1558 Kroupa, P. 2001, From Darkness to Light: Origin and
     Evolution of Young Stellar Clusters, 243, 1.
     https://arxiv.org/abs/0010405v2
1561 Kuhn, M. A., Medina, N., Getman, K. V., et al. 2017
1562 Kuhn, M. A., Feigelson, E. D., Getman, K. V., et al. 2014,
     Astrophysical Journal, 787,
     doi: 10.1088/0004-637X/787/2/107
   Lindegren, L. 2019, arXiv,
     doi: 10.1051/0004-6361/201936161
   Lindegren, L., Hernández, J., Bombrun, A., et al. 2018,
     Astronomy and Astrophysics, 616, 1,
     doi: 10.1051/0004-6361/201832727
   Lindegren, L., Bastian, U., Biermann, M., et al. 2020, Gaia
     Early Data Release 3: Parallax bias versus magnitude,
     colour, and position. http://arxiv.org/abs/2012.01742
1574 Liu, L., & Pang, X. 2019. http://arxiv.org/abs/1910.12600
1575 Luri, X., Brown, A. G., Sarro, L. M., et al. 2018,
     Astronomy and Astrophysics, 616, 1,
     doi: 10.1051/0004-6361/201832964
1578 McKinney, W. 2010, Proceedings of the 9th Python in
     Science Conference, 1, 56,
     doi: 10.25080/majora-92bf1922-00a
     -. 2011, Python for High Performance and Scientific
   Olivares, J., Bouy, H., Sarro, L. M., et al. 2019, Astronomy
     and Astrophysics, 625, A115,
     doi: 10.1051/0004-6361/201834924
   Pang, X., Li, Y., Yu, Z., et al. 2021,
```

```
1588 Pearson, K. 1893, Bulletin of Mathematical Biology, 185,
                                                                    1612 Sim, G., Lee, S. H., Ann, H. B., & Kim, S. 2019, Journal of
      doi: https://doi.org/10.1098/rsta.1894.0003
1589
                                                                          the Korean Astronomical Society, 52, 145,
                                                                    1613
1590 Pedregosa, F., Varoquaux, G., Buitinck, L., et al. 2015,
                                                                          doi: 10.5303/JKAS.2019.52.5.145
      GetMobile: Mobile Computing and Communications, 19,
1591
                                                                    1615 Skrutskie, M. F., Cutri, R. M., Stiening, R., et al. 2006, The
      29, doi: 10.1145/2786984.2786995
1592
                                                                          Astronomical Journal, 131, 1163, doi: 10.1086/498708
    Perets, H. B. 2015, 251–275,
1593
      doi: 10.1007/978-3-662-44434-4{_}11
                                                                    1617 Spina, L., Ting, Y.-S., De Silva, G. M., et al. 2021, Monthly
1594
   Perez, F., & Granger, B. E. 2007, Computing in Science &
1595
                                                                          Notices of the Royal Astronomical Society, 503, 3279,
      Engineering, 9, 21, doi: 10.1109/MCSE.2007.53
1596
                                                                          doi: 10.1093/mnras/stab471
                                                                    1619
    Price-Whelan, A. M., Nidever, D. L., Choi, Y., et al. 2019,
1597
                                                                    1620 Toonen, S., Portegies Zwart, S., Hamers, A. S., &
      The Astrophysical Journal, 887, 19,
1598
                                                                          Bandopadhyay, D. 2020, arXiv, 16
      doi: 10.3847/1538-4357/ab4bdd
                                                                    1621
1599
    Price-Whelan, A. M., Sipőcz, B. M., Günther, H. M., et al.
1600 I
                                                                        Utsunomiya, M., Hashimoto, M., & Kajitani, H. 1996, NEC
                                                                    1622
      2018, The Astronomical Journal, 156, 123,
1601
                                                                          Research and Development, 37, 369
      doi: 10.3847/1538-3881/aabc4f
1602
                                                                        Vasiliev, E. 2019, Monthly Notices of the Royal
                                                                    1624
    Prusti, T., de Bruijne, J. H. J., Brown, A. G. A., et al.
1603
                                                                          Astronomical Society, 489, 623,
                                                                    1625
      2016, Astronomy & Astrophysics, 595, A1,
1604
      doi: 10.1051/0004-6361/201629272
                                                                          doi: 10.1093/mnras/stz2100
1605
                                                                    1626
   Riello, M., De Angeli, F., Evans, D. W., et al. 2018,
1606
                                                                        Virtanen, P., Gommers, R., Oliphant, T. E., et al. 2020,
      Astronomy and Astrophysics, 616, 1,
1607
                                                                          Nature Methods, 17, 261, doi: 10.1038/s41592-019-0686-2
                                                                    1628
      doi: 10.1051/0004-6361/201832712
1608
                                                                        Wenger, M., Ochsenbein, F., Egret, D., et al. 2000, 22, 9,
                                                                    1629
    Robitaille, T. P., Tollerud, E. J., Greenfield, P., et al. 2013,
1609
                                                                          doi: 10.1051/aas:2000332
      Astronomy & Astrophysics, 558, A33,
1610
      doi: 10.1051/0004-6361/201322068
1611
```